Towards Low-Latency Estimation of Atmospheric CO_2 Growth Rates using Satellite Observations: Evaluating Sampling Errors of Satellite and In Situ Observing Approaches

Sudhanshu Pandey[1], John B. Miller[2], Sourish Basu[3,4], Junjie Liu[1,5], Brad Weir[3,6], Brendan Byrne[1], Frédéric Chevallier[7], Kevin W. Bowman[1,8], Zhiqiang Liu[9], Feng Deng[10], Christopher W. O'Dell[11], Abhishek Chatterjee[1]

[1]Jet Propulsion Laboratory, California Institute of Technology, Pasadena, CA, USA
[2]NOAA Global Monitoring Laboratory, Boulder, CO, USA
[3]NASA Goddard Space Flight Center, Global Modeling and Assimilation Office, Greenbelt, MD, USA
[4]Earth System Science Interdisciplinary Center, College Park, MD, USA
[5]Division of Geological and Planetary Sciences, California Institute of Technology, Pasadena, CA, USA
[6]Morgan State University, Baltimore, MD, USA
[7]Laboratoire des Sciences du Climat et de L'Environnement, LSCE/IPSL, CEA-CNRS-UVSQ, Université Paris-Saclay, 91191 Gif-sur-Yvette, France
[8]Joint Institute for Regional Earth System Science and Engineering, University of California, Los Angeles, CA, USA
[9]CMA Key Open Laboratory of Transforming Climate Resources to Economy, Chongqing Institute of Meteorological Sciences, Chongqing, 401147, China
[10]Department of Physics, University of Toronto, Toronto, Ontario, Canada
[11]Cooperative Institute for Research in the Atmosphere, Colorado State University, Fort Collins, CO, USA

Correspondence: Sudhanshu Pandey (sudhanshu.pandey@jpl.nasa.gov)

Abstract: The atmospheric CO_2 growth rate is a fundamental measure of climate forcing. NOAA's growth rate estimates, derived from in situ observations at the marine boundary layer (MBL), serve as the benchmark in policy and science. However, NOAA's MBL-based method encounters challenges in accurately estimating the whole-atmosphere CO_2 growth rate at sub-annual scales. We introduce the Growth Rate from Satellite Observations (GRESO) method as a complementary approach to estimate the whole-atmosphere CO_2 growth rate utilizing satellite data. Satellite CO_2 observations offer extensive atmospheric coverage that extends the capability of the current NOAA benchmark. We assess the sampling errors of the GRESO and NOAA methods using ten atmospheric transport model simulations. The simulations generate synthetic OCO-2 satellite and NOAA MBL data for calculating CO_2 growth rates, which are compared against the global sum of carbon fluxes used as model inputs. We find good performance for the NOAA method (R = 0.93, RMSE = 0.12 ppm $year^{-1}$

or 0.25 PgC year^{-1}). GRESO demonstrates lower sampling errors (R = 1.00; RMSE = 0.04 ppm year^{-1} or 0.09 PgC year^{-1}). Additionally, GRESO shows better performance at monthly scales than NOAA (R = 0.77 vs 0.47, respectively). Due to CO_2's atmospheric longevity, the NOAA method accurately captures growth rates over five-year intervals. GRESO's robustness across partial coverage configurations (ocean or land data) shows that satellites can be promising tools for low-latency CO_2 growth rate information, provided the systematic biases are minimized using in situ observations. Along with accurate and calibrated NOAA in situ data, satellite-derived growth rates can provide information about the global carbon cycle at sub-annual scales.

1 Introduction

Accurate estimations of atmospheric CO_2 abundance and growth rates are vital for climate monitoring, predictions, and policymaking. Since the pre-industrial times, the global mean abundance of CO_2 has increased by more than 50%, rising from 278 parts per million (ppm) to 419 ppm as of September 2023 (Lan et al., 2023). CO_2 is the most significant anthropogenic greenhouse gas, contributing to approximately 66% of the radiative forcing by long-lived greenhouse gases. It has been responsible for an 80% increase in radiative forcing over the last decade (WMO, 2022).

The change in the number of atmospheric CO_2 molecules for any time interval is equal to the global net surface flux of CO_2 over the same interval. CO_2 has negligible atmospheric chemical destruction and a small amount of atmospheric chemical production from carbon monoxide (~ 0.2 PgC vs. an atmospheric CO_2 burden of ~ 850 PgC). Moreover, atmospheric chemical production generally has low interannual and intra-annual variability, leading to negligible influence on global growth rates.

Figure 1 displays the estimated growth rate of CO_2 for recent decades estimated from monthly global CO_2 mean values from the National Oceanic and Atmospheric Administration (NOAA) using Marine Boundary Layer (MBL) atmospheric CO_2 observations. Emissions from anthropogenic activities, such as fossil fuel combustion, cement production, and land-use changes, are also shown. Anthropogenic sources are estimated to have emitted 11 petagrams of carbon (PgC) in 2021 (Friedlingstein et al., 2022a). The land biosphere and ocean act as net sinks for CO_2, absorbing, on average, about half of the emissions from human activities. These sinks are sensitive to major climate variation modes such as the El Niño-Southern Oscillation (ENSO) (Bacastow, 1976). The total sink, comprising land and ocean sinks, varies from 20% to 80% of annual anthropogenic emissions. The land sink shows substantial interannual variability, influenced by the balance between photosynthetic CO_2 uptake, respiratory release, and fires. Although much smaller in magnitude, variations in ocean fluxes also impact the interannual CO_2 growth rate (Feely et al., 1999; Chatterjee et al., 2017). The proportion of anthropogenic CO_2 that remains in the atmosphere, known as the airborne fraction (AF), drives variations of the atmospheric growth rates,

which can reveal trends in the carbon cycle (Knorr, 2009; Ballantyne et al., 2012; Van Marle et al., 2022; Bennedsen et al., 2023). Accurate estimation of CO_2 growth rates is essential for evaluating the climate sensitivity of land carbon fluxes in Earth system models and reducing uncertainty in climate predictions (Cox et al., 2013; Barkhordarian et al., 2022).

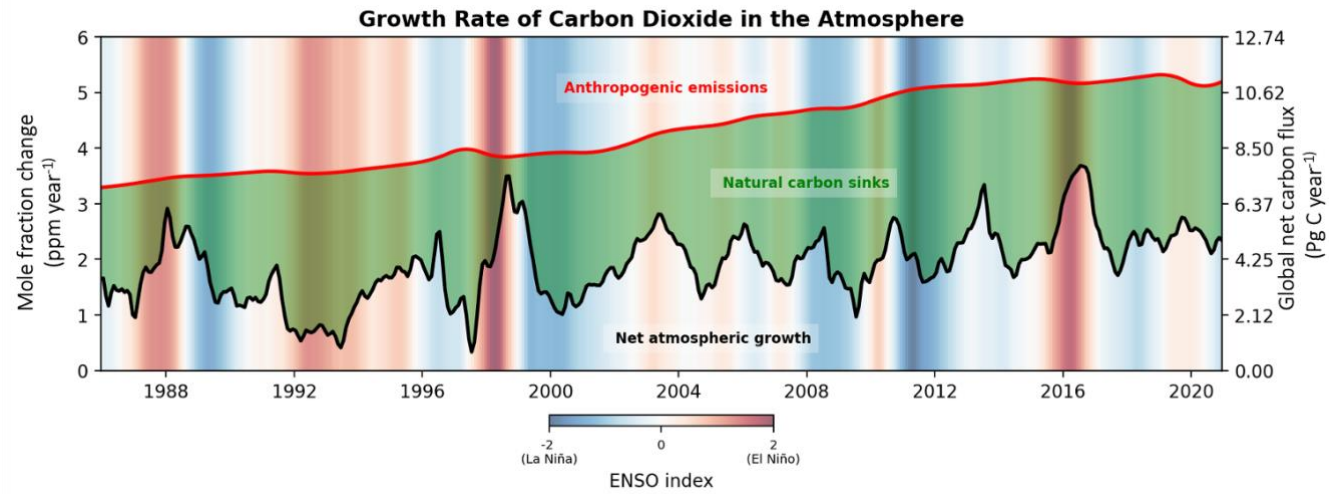

Figure 1. Fossil fuel and other anthropogenic CO_2 emissions vs. atmospheric growth rate of CO_2. The growth rate time series (black line) is calculated from deseasonalized monthly global MBL CO_2 mole fraction estimates provided by NOAA (Lan et al., 2023). To underscore the significant variability in the natural carbon sink, monthly growth rates are shown instead of the more accurate officially reported annual growth rates from NOAA. The anthropogenic CO_2 emissions (red line) are taken from the Global Carbon Project (Friedlingstein et al., 2022a). The emissions are interpolated to monthly scales, employing a cubic spline fit. The background vertical shading corresponds to the monthly-resolution Multivariate ENSO Index (MEI; Wolter et al., 2011). The area shaded in green represents the removal of CO_2 by land and ocean sinks. Tick marks on the right-hand y-axis represent the equivalent global net CO_2 fluxes, expressed in units of PgC $year^{-1}$.

Continuous observations of CO_2 at remote background sites (Mauna Loa and the South Pole) commenced in the 1950s by the Scripps Institution of Oceanography. Within the large seasonal and latitudinal variations, these CO_2 observations revealed a "small but persistent growth in concentration" (Keeling, 1960). To monitor this growth, NOAA's Global Monitoring Laboratory (GML) established the Global Greenhouse Gas Reference Network (GGGRN), which collects flask air samples from 50 remote sites globally (Figure 2) in addition to numerous sites on various platforms over the continents. The NOAA growth rate estimation method employs in situ CO_2 observations from the MBL observation sites in their network to estimate growth rates of CO_2, and other trace gases such as methane and nitrous oxide (CCGCRV, 2023; Lan et al., 2023; Masarie and Tans, 1995). These growth rates represent the longest continuous record of direct observations of global CO_2 changes as a function of latitude, with the extended NOAA network dating back to the mid-1970s.

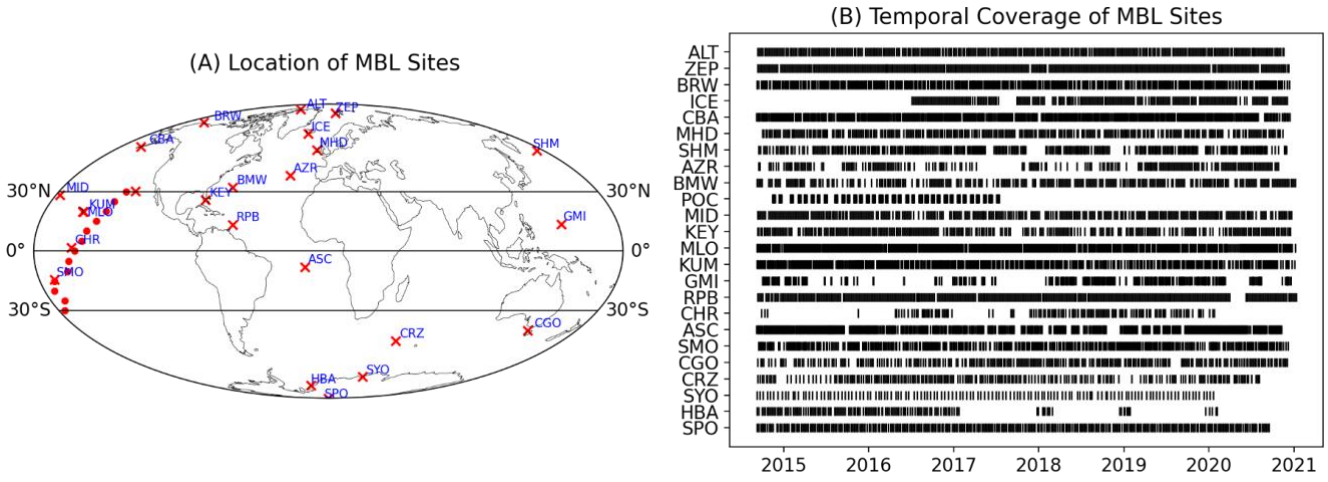

Figure 2. Coverage of NOAA MBL in situ flask-air observations for 2015-2020. Panel A illustrates the locations of MBL sites. Crosses indicate ground-based sites, whereas shipboard measurements in the Pacific Ocean are represented by dots, corresponding to the locations of those measurements for growth rate calculations. Panel B delineates the temporal extent of CO_2 flask observations for each site. The temporal coverage of all shipborne observations in the Pacific is aggregated and represented under a single label designated as POC.

NOAA's growth rates are the current benchmark, widely utilized in policy and scientific contexts, for example, providing the foundation for the Global Carbon Budget Project (Friedlingstein et al., 2022a). However, the MBL in situ observation network is limited to surface measurements at remote marine locations. This incomplete sampling of the whole atmosphere impacts NOAA's growth rate estimates due to the combined effect of (1) interannual variations in CO_2 fluxes, atmospheric transport mechanisms that connect these fluxes to observations, and (2) the lack of representation of the vertical component of the atmosphere (Pandey et al., 2019). Thus, NOAA's MBL CO_2 abundance and growth rate estimates can be considered to be strictly valid for the MBL, not the entire atmosphere, even though these MBL values are implicitly used as proxies for both whole-atmosphere CO_2 abundance and growth. NOAA's MBL CO_2 uncertainty estimates (Ballantyne et al., 2012; and described below in the Methods) account for incomplete sampling, but only with respect to the distribution of sites within the MBL and cannot be considered uncertainties for representing the whole atmosphere.

Surface network data may not precisely reflect the true, mass-weighted whole-atmosphere average CO_2 mole fraction due to the limitations of vertical and horizontal mixing. The CO2 increase in the stratosphere trails behind that in the marine boundary layer, while concentrations in the continental boundary layer typically lead, often offsetting each other (Ballantyne et al., 2012). Therefore, whole-atmosphere inaccuracies are minimal over spans of 5 to 10 years due to atmospheric mixing and the very long atmospheric lifetime of CO_2. However, residual inaccuracies remain at the annual scale, necessitating further examination, as recognized by the Global Carbon Budget 2021 paper (Friedlingstein et al., 2022a).

NOAA publishes annual CO_2 growth rates for each year in April of the following year, a four-month latency primarily due to two factors. Firstly, the growth rate for a calendar year can only be determined several months into the subsequent year, as flask-air samples need to be shipped to NOAA GML's Boulder laboratory from very remote sampling locations. Secondly, the estimated growth rate for a given year is subject to "end effects" in the trend curve calculations that need approximately four months to begin to stabilize (see Figure 9/Section 4.5).

Science and policy applications could benefit from the availability of growth rates with lower latency and better temporal resolution than annual values. Fine-temporal-resolution global growth rates can serve as a valuable tool for the immediate tracking of anthropogenic and biospheric carbon fluxes amid climatic irregularities such as droughts, heatwaves, and floods. For instance, the impact of the COVID-19 pandemic on CO_2 growth rates was being investigated concurrently with the event (Weir et al., 2021; Laughner et al., 2021). Similarly, the 2015-2016 El Niño effects were studied in real-time (Chatterjee et al., 2017; Liu et al., 2017). This is also relevant for areas prone to aggressive climate shifts (William et al., 2022). Monthly-to-seasonal-scale regional events affect the global CO_2 growth rate. For example, the 2023 Canadian fires released between 572–705 Tg C over five months (Byrne et al., 2023). The significant flux signal might have been observable in sub-annual CO_2 growth rates, which are challenging to estimate using the current MBL in situ network. The rapid availability of satellite data can facilitate low-latency estimations of growth rates, which can be used as a preliminary low-latency measure of extreme climate incidents, allowing for monitoring well in advance of the more intricate outputs derived from sophisticated atmospheric inverse models or biosphere models. Satellite observations provide more extensive atmospheric sampling and low-latency data, but their use has not been fully explored to calculate growth rates.

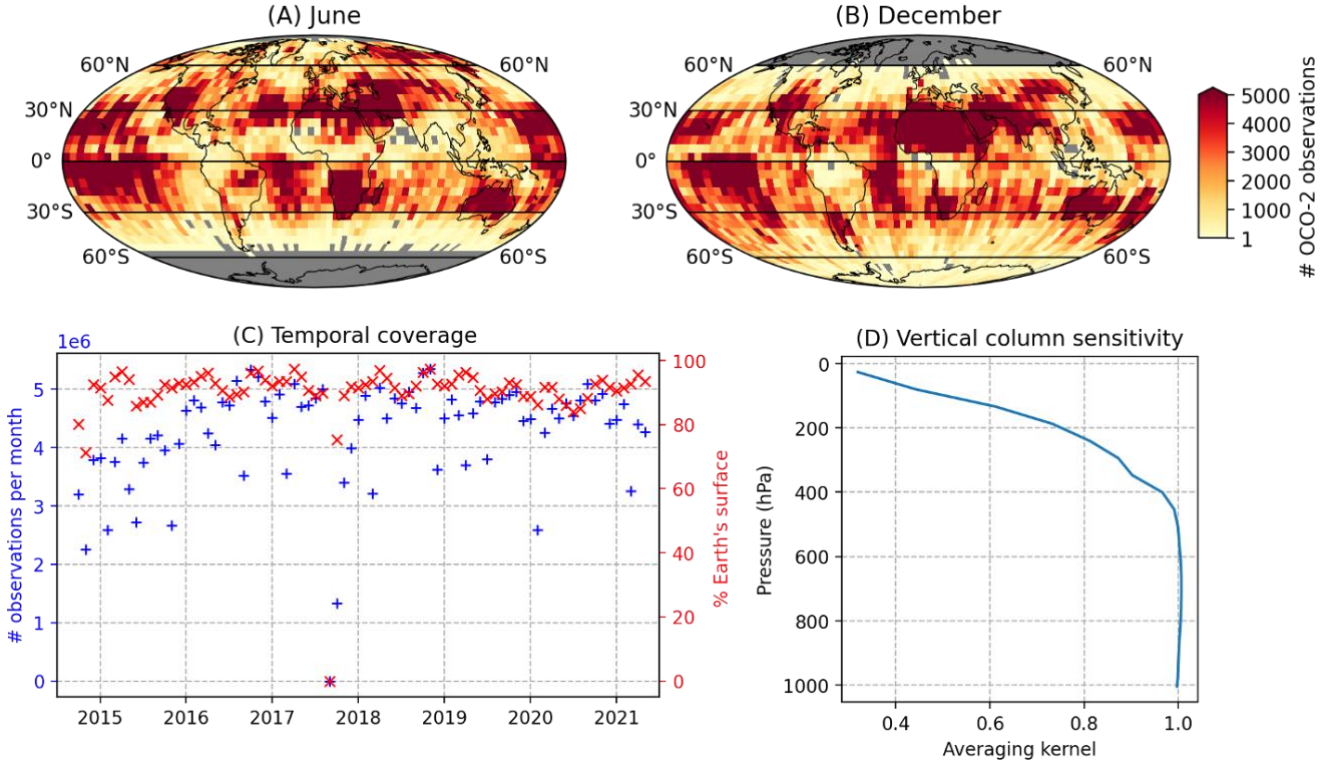

Figure 3. The spatial and temporal coverage of OCO-2 CO_2 observations. Panels A and B illustrate the number of single-sounding observations per 5° × 5° grid cell (latitude and longitude) for June and December 2018, respectively, representing the typical extremes in seasonal coverage patterns. Panel C displays the number of observations per month, denoted by blue '+' symbols, and the percentage of Earth's area covered by filled 5° × 5° grids with observations, denoted by red '×' symbols. Panel D depicts a typical averaging kernel for OCO-2, which describes the sensitivity of a CO_2 observation as a function of pressure. The figure is discussed in Sections 2 and 3.2.

The Orbiting Carbon Observatory-2 (OCO-2) satellite, launched in July 2014, measures column-average dry-air mole fractions of CO_2 (i.e., moles of CO_2 per mole of dry air, typically expressed as ppm), commonly denoted as XCO_2, with near-global coverage (Crisp et al., 2017; Eldering et al., 2017). Figure 3 shows the coverage of OCO-2. Satellite measurements have wider horizontal coverage than the MBL in situ observations used by NOAA. Also, satellite measurements utilize CO2 bands in the shortwave infrared (SWIR), which are sensitive to CO_2 throughout the troposphere and partially sensitive in the stratosphere (Figure 3D). Above the tropopause, where the averaging kernel deviates from unity, CO_2 abundance information is derived in part from a priori CO_2 profiles so that total column abundance can be estimated. Some studies have attempted to estimate growth rates using satellite data. For example, Buchwitz et al. (2018) published growth rates from combined SCIAMACHY-ENVISAT and GOSAT, and National Institute for Environmental Studies publishes growth rates from GOSAT data (NIES, 2023).

Despite the better atmospheric coverage of satellites, the lower accuracy and precision of XCO_2 relative to in situ measurements may yield satellite-derived growth rates with greater uncertainty than NOAA estimates. The current level of trust in growth rates derived from satellite observations, or even from atmospheric flux inversions, does not match the confidence in global growth rates provided by NOAA. Growth rates, or 3D mole fraction fields based on inverse-posterior fluxes, are still validated against NOAA MBL-based estimates (Buchwitz et al., 2018; Taylor et al., 2023; Byrne et al., 2023). The advantage of better atmospheric coverage by satellite in reducing sampling errors remains unknown.

We present a new method, the Growth Rate from Satellite Observations (GRESO), which is tailored for determining growth rates using satellite data. While the GRESO method draws on the NOAA approach, it is specifically optimized to leverage the enhanced atmospheric sampling capabilities of satellites. The error in real-world growth rates derived from satellite data will be the quadratic sum of the sampling errors and the biases that remain uncorrected by the bias correction schemes. This study focuses only on understanding and minimizing atmospheric sampling errors. Using Observing System Simulation Experiments (OSSEs), we evaluate the whole-atmosphere sampling uncertainties inherent in the NOAA and GRESO methods.

The rest of this paper is structured as follows: Section 2 explores the concept of CO_2 growth rate, details the NOAA method, and introduces the GRESO method. Section 3 provides a deeper look into our data and methodology, including using the OSSE approach to estimate errors in growth rate methods. Section 4 unveils our results and discussion, examining our OSSE results and the sampling errors linked to NOAA and GRESO estimates. Following this, we present a series of stress tests using the OSSE setup to evaluate the robustness of the GRESO method. Additionally, we briefly touch on other methods of growth rate estimates. After that, we discuss the delay in the availability of these estimates. Section 5 gives the summary and outlook.

2 Growth rate estimation methods

A growth rate method estimates the change in globally averaged mole fraction of CO_2. The growth rate $G_{ATM}\ (t_1, t_2)$ over a period $t_1 - t_2$ can be calculated as follows:

$$G_{ATM}(t_1, t_2) = k \frac{M_{ATM}(t_2) - M_{ATM}(t_1)}{t_2 - t_1}, \quad \ldots\ldots\ldots (1)$$

where $M_{ATM}\ (t)$ is the whole-atmosphere average mole fraction in ppm, i.e., the total number of CO_2 molecules in the atmosphere divided by the total number of air molecules after removal of the water vapor component. The constant k = 2.124

PgC ppm^{-1} serves as a conversion factor. It is derived assuming (instantaneous) dilution of a unit amount of CO_2 into the entire atmosphere (Ballantyne et al., 2012; Friedlingstein et al., 2022a).

A growth rate method calculates the time series $M_{ATM}(t)$ using a set of discrete atmospheric CO_2 observations (Z) of the continuous four-dimensional CO_2 mole fraction field $m(l_x, l_y, h, t)$, where l_x , l_y, h are longitude, latitude, and the geopotential height, respectively. $M_{ATM}(t)$ approximates the true density-weighted average of the mole fraction field, $\bar{m}(t)$, across l_x , l_y and h:

$$M_{ATM}(t) = \bar{m}(t) + \epsilon(t), \ldots\ldots\ldots \quad (2)$$

where, $\epsilon\ (t)$ denotes the error, comprising the measurement error, sampling error (the error due to incomplete sampling of the mole fraction field), and model theory error associated with the growth rate method. The net flux of CO_2 into or out of the atmosphere is equal to $k\frac{d\bar{m}(t)}{dt}$. While the atmospheric chemical production of CO_2 (mainly via oxidation of CO by OH) is not negligible in any given year, its year-to-year variability and, thus, contribution to $\frac{d\bar{m}(t)}{dt}$ is negligible. $\epsilon(t)$ can be decomposed into time-dependent error component $\alpha(t)$, with mean of zero, and time-invariant error components β:

$$\epsilon(t) = \alpha_b(t) + \alpha_r(t) + \beta_b + \beta_r \quad \ldots\ldots\ldots \quad (3)$$

The subscripts *b* and *r* represent the systematic and random components of the error, respectively. When calculating G_{ATM}, the β error terms of M_{ATM} cancel out as per Equation 1. The random error component $\alpha_r(t)$ is not a major contributor to the overall error owing to a large number of measurements used. Typically, the analytical random error is about 0.10 ppm for in situ observations and about 0.5 ppm for satellite observations. A growth rate method uses thousands of observations, so the random errors are diminished quickly following of the law of large numbers, for all practical purposes. The main error sustained when calculating growth rates $G_{ATM}(t_1, t_2)$ results from $\alpha_b(t_1)$ and $\alpha_b(t_2)$. It comprises (1) sampling errors due to absolute and year-to-year changes in observations coverage, and (2) temporally varying observations biases or *growth rate biases* in observations. Growth rate methods are designed to minimize the sampling error component of $\alpha_b(t)$, but errors due to growth rate biases in retrievals as well as in situ observations are difficult to address.

2.1 The NOAA growth rate method

CO_2 observations at each NOAA MBL site exhibit a seasonal cycle, long-term trend, and noise attributable to local influences (Keeling, 1960). NOAA reports annual growth rate estimates using a combination of filtering, deseasonalization, interpolation, and data-extension techniques (Masarie and Tans, 1995). The method first creates a continuous, smoothed, and

deseasonalized weekly CO_2 time series for each MBL measurement site, $M_{site}(t)$ (Thoning et al., 1989). For each site, the measurements ($Z_{site}(t)$) are fitted to a function using least squares minimization of residuals to a function composed of a quadratic polynomial $\phi_p(t)$ to capture the long-term trend, along with a harmonic function $\phi_{\mathrm{h}}(\mathrm{t})$ with eight harmonic parameters to represent the average seasonal cycle as follows.

$$Z_{site}(t) = \phi_p(t) + \phi_{\mathrm{h}}(\mathrm{t}) + R(t)$$

$$\phi_p(t) = c_0 + c_1 t + c_2 t^2$$

$$\phi_h(\mathrm{t}) = \sum_{k=1}^{4} [b_{2k-1} \sin(2\pi k t) + b_{2k} \cos(2\pi k t)] \quad \ldots\ldots\ldots (4)$$

After determining the coefficients for the polynomial and harmonic functions, the residuals $R(t)$ are computed by subtracting the function values from the original dataset ($R(t) = Z_{site}(t) - \phi_p(t) - \phi_h(t)$). These residuals are then filtered twice (in the frequency domain), once using a low-pass filter with a cutoff frequency typically set to a value equivalent to 80 days and once with a cutoff equivalent to 667 days. The short filter is intended to remove higher frequency noise, for example, associated with synoptic-scale variability, and capture interannual variations in seasonality not captured by the initial least-squares fit. The long filter is intended to remove any remaining seasonal variability as well as some interannual variability and thereby isolate longer-term trends. The smoothed residuals are then transformed back into the time domain via an inverse Fast Fourier Transform. $M_{site}(t)$ is generated using the "trend curve", which is the sum of $\phi_p(t)$ and $R(t)$ filtered with the large cutoff value (CCGCRV, 2023). Additionally, as first described by Masarie and Tans, (1995), a "difference" climatology (comparing adjacent sites) is used to fill in long gaps in measurement time series at any given site. The set of fully gap-filled time series from all sites is then synchronized to 48 "quasi-weeks" per year. This gap-filling and synchronization process results in "extended" data records, which form the basis for calculating global, annual mean CO_2 (and other long-lived GHGs).

Then, for each quasi-week, CO_2 values from all sites are fitted meridionally. The fitted curve is then sampled in forty-one 0.05 sine of latitude (equal area) increments (Tans et al., 1989). This process results in a matrix with dimensions of 41 by 48 by the number of years, representing the north-south and temporal distribution of MBL CO_2. A time-dependent global mean MBL CO_2 is then calculated simply by averaging along the north-south dimension. Annual growth rates are determined by subtracting the mean values for December and January (abbreviated as MDJ) of one year from the MDJ values of the following year as a way of suppressing some noise (as opposed to interpolating the quasi-week values to January 1). This calculation approximates the net amount of CO_2 added to or removed from the atmosphere due to both anthropogenic emissions and net land and ocean sinks over the course of the year. The method approximates global mean MBL CO_2 to represent the whole-atmosphere CO_2 mole fraction ($M_{MBL}(t) \sim M_{ATM}(t)$). Previous tests with inverse model-generated three-dimensional distributions of atmospheric CO_2 have shown that the MBL is a good proxy for the whole-atmosphere

CO_2 abundance, due to the cancellation of errors by not representing the continental boundary layer, with higher CO_2 generally, and not representing the stratosphere, with lower CO_2 (see Methods of Ballantyne et al., 2012).

To evaluate the sampling error of the MBL portion of the GGGRN, NOAA employs a bootstrap method, generating 100 alternative global networks from existing NOAA/GML MBL sites (Conway, 1994). Each of these alternative networks maintains the same number of sites but may contain duplicates or omissions. Furthermore, each network is required to include at least one site from the southern, tropical, and northern high latitudes. These alternative networks also retain their temporal data gaps. Starting in September 2018, NOAA introduced an additional term for analytical uncertainty, calculated using a Monte Carlo method. NOAA-reported growth rate uncertainties are based primarily on the spread (the inner 68th percentile) of the bootstrap ensemble. Measurement uncertainty constitutes a small component of the total uncertainty, particularly in the timeframe examined in this study (Ballantyne et al., 2012). The globally averaged surface CO_2 concentrations, both monthly and annual means, along with annual growth rates, are made publicly available on the NOAA webpage (Lan et al., 2023).

2.2 Growth rate from satellite observations (GRESO) method

Figure 4 lists the main steps of the GRESO method. The GRESO method can be divided into two groups of processing steps: (1) sequential aggregation and (2) time series processing.

Sequential aggregation generates a representative global CO_2 mole fraction time series $M_{ATM}(t)$ from individual OCO-2 soundings. This process uses stepwise averaging and data elimination to ensure that areas with high numbers of observations or high errors do not overly influence the global CO_2 mole fraction time series. The OCO-2 soundings have a footprint size of 1.25 km x 2.2 km. They are first converted into 10-second average OCO-2 XCO_2 (referred to as 10s XCO_2 observations hereafter). Mean XCO_2 observations over 10-second intervals (equivalent to about 67.5 km along the satellite's trajectory) are calculated by weighting based on the inverse of the square of the XCO_2 uncertainty from the retrieval. To consider the potential correlations between individual measurements, assumed correlations of +0.3 for land scenes and +0.6 for ocean scenes are incorporated in calculating the mean and uncertainty for the 10s averages. The measurements with lower uncertainties contribute more to the final 10s average than those with higher uncertainties. For a detailed description of this approach, see Baker et al. (2022).

In the subsequent step, poor-quality 10s data are filtered out. Initially, measurements with uncertainties exceeding two ppm are discarded. Additional filtering is implemented to eliminate unrealistic XCO_2 values for well-mixed atmospheric CO_2. The 10s data are grouped into 16-day intervals, and XCO_2 values deviating by more than five standard deviations from the

group's median are discarded. This procedure aids in removing unrealistic XCO_2 values in the CO_2 field of a well-mixed atmosphere.

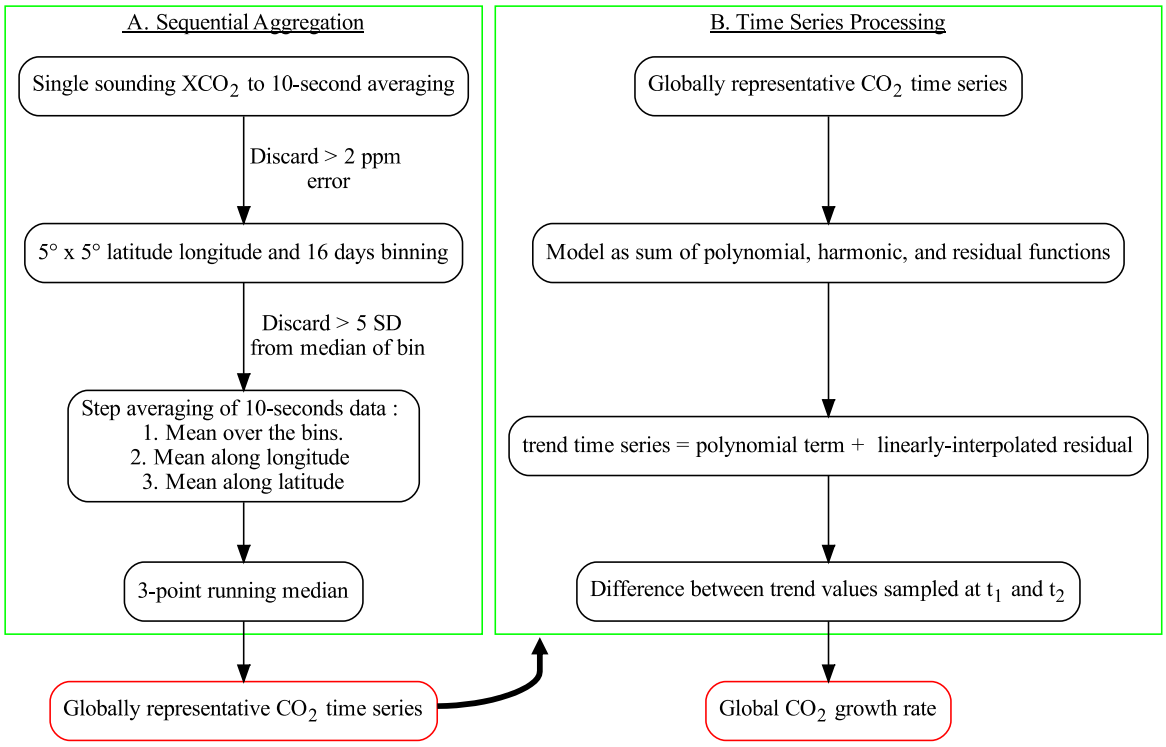

Figure 4. Schematic flowchart of the growth rate from satellite observations (GRESO) method.

The remaining 10s XCO_2 data are then processed by averaging them onto a grid with a resolution of 5° latitude by 5° longitude and a temporal resolution of 16 days. This results in a three-dimensional array with dimensions for latitude, longitude, and time. The average CO_2 mole fraction along the longitude dimension is then calculated, producing a two-dimensional array of CO_2 mole fraction time series for each 5° latitude band. After that, averaging is performed along the latitude dimension, weighted with the cosine of latitude to account for the changes in meridional atmospheric airmass. This results in a time series of globally representative CO_2 mole fractions. This time series is smoothed using a running 3-point median to give the global CO_2 time series M_{ATM}, with a temporal resolution of 16 days.

The time series processing steps are as follows. M_{ATM} is interpolated for missing data points in the time domain and then, both annual and deseasonalized monthly CO_2 growth rates are calculated. M_{ATM} is modeled as a sum of polynomial, harmonic, and residual functions using the method described by Equation 4. This deseasonalized version of the global CO_2 time series ($M_{ATM,D}\ (t)$) is then obtained by adding only the polynomial term and a linearly interpolated residual function, $M_{ATM,D}(t) = \phi_p(t) + R(t)$. Thereafter, $M_{ATM,D}\ (t)$ is sampled at the beginning of each calendar month. The difference in CO_2 concentrations between consecutive time steps is used to obtain the monthly growth rate in ppm month^{-1} (Equation 1). Averaging the growth rates of each month within a year yields the annual growth rate, which represents the CO_2 growth rate from midnight of December 31st of the preceding year to midnight of December 31st of the current year. This annual growth rate is equivalent to the sum of all the monthly CO_2 fluxes during that year. Note that because the monthly growth rates are calculated from deseasonalized global CO_2 time series, they do not have a seasonal cycle.

3. Method and Data

To understand the sampling errors of the NOAA and GRESO methods, we design OSSEs using posterior (optimized) three-dimensional estimates of CO_2 mole fractions from atmospheric CO_2 inversions from the OCO-2 version 10 Model Intercomparisons Project (MIP; Byrne et al., 2023). For each MIP model run used here, the estimated total surface CO_2 flux over any time interval is known and identically matches the estimated change in whole-atmosphere CO_2 abundance over the same interval. Growth rates from these methods are estimated by sampling the posterior mole fraction fields at the times and locations of the true MBL flask-air and OCO-2 soundings ("co-samples"), with OSSE "truth" defined as the posterior fluxes of the MIP inversions.

3.1 NOAA point measurements

NOAA's Global Monitoring Laboratory (GML) monitors atmospheric CO_2 abundance in the remote surface atmosphere as part of its GGGRN (Conway et al., 1994). The network is an international collaborative effort which includes regular discrete flask-air samples from the GML baseline observatories, cooperative fixed sites, and commercial ships (Figure 2). Air samples are collected in 2.2 L borosilicate flasks approximately weekly from these globally distributed networks of sites. The flasks are measured in GML's Boulder laboratory for dry air mole fraction of CO_2, reported in ppm. Because the atmospheric gradients of CO_2 are small in the background atmosphere far from sources of pollution, the World Meteorological Organization (WMO) Global Atmosphere Watch (GAW) has adopted a single reference scale (currently X2019; Hall et al., 2021), maintained and disseminated by NOAA, upon which to base all measurements made within the program. The scale is based on the International System of Units (called "SI") and is recognized by the International Bureau of Weights and Measures (BIPM), the coordinating body of metrology laboratories. NOAA participates in regular comparisons of standards for "Amount of Substance Ratios" (mole fractions) for greenhouse gases organized by the BIPM.

Most, but not all, CO_2 mole fraction measurements are calibrated to the NOAA scale. The WMO mole fraction scale is also the target CO_2 scale to which remote sensing measurements such as those from TCCON and OCO-2 are linked via calibrated in situ measurements.

3.2 OCO-2 observations

The OCO-2 satellite operates in a sun-synchronous, near-polar orbit at an altitude of 705 km. Its equatorial crossing time is between 13:21 and 13:30 local time, with ground tracks more closely spaced at high latitudes than at mid-latitudes. As part of the Earth Observing System's (EOS) Afternoon Constellation (A-Train), OCO-2 has a 16-day ground track repeat cycle providing global XCO_2 coverage twice a month. OCO-2 is equipped with a spectrometer that measures sunlight reflected by the Earth and its atmosphere in three spectral bands: the oxygen A-band in the near-infrared (NIR) at 0.76 μm wavelength and two CO_2 spectral bands in the shortwave infrared (SWIR) at 1.6 and 2.1 μm. The satellite offers spatially dense data with a narrow 10 km swath and a spatial resolution of 1.25 km by 2.2 km. Land and ocean XCO_2 retrievals from OCO-2 are performed using version 10 of NASA's Atmospheric CO_2 Observations from Space (ACOS) full-physics retrieval algorithm (O'Dell et al., 2018). OCO-2 data are validated and bias-corrected using CO_2 retrievals from the Total Column Carbon Observing Network (TCCON; Wunch et al., 2017; Taylor et al., 2023), whose data have been linked to the WMO CO_2 mole fraction scales via calibrated in situ vertical profiles sampled by aircraft and AirCore (Karion et al., 2010; Laughner et al., 2023b).

Figure 3 displays coverage of single-sounding OCO-2 observations from September 2014 to June 2021. Approximately two-thirds of OCO-2 observations are from ocean glint mode, while 16% are land nadir, 16% are land glint, and only 0.05% are land target observations. Nadir retrievals are those in which the satellite looks at the Earth directly below, i.e., at the sub-satellite point. These retrievals are only usable when the instrument is directly over land. Glint retrievals are from measurements occurring when the instrument is pointed (usually off-nadir) toward the solar glint spot. Glint is the primary mode for over-ocean retrievals, as the ocean surface is very dark in the SWIR spectral range when viewed from the nadir, only reflecting sufficient solar radiation near the glint point. Target mode retrievals are obtained when the sensor points at a fixed location along the orbit to keep a particular point on the Earth's surface in view. Target mode is employed mainly to collect validation data over locations such as TCCON sites.

Due to OCO-2's reliance on sunlight, the coverage gaps at high latitudes vary seasonally, with reduced coverage during winter months in each hemisphere (Figure 3A and 3B). These gaps are most noticeable during solstices when the Earth's tilt results in the poles experiencing their longest periods of darkness. From 2015 to 2021, OCO-2 covered approximately 80% of the Earth's surface in most months. We determine the monthly area coverage by calculating the fraction of 5° x 5° grid cells with at least one satellite observation during the month. From July 31–September 19, 2017, OCO-2 data collection was

suspended. Having a low number of observations in a month does not necessarily imply low area coverage, as area coverage measures the extent of observations over the month. For instance, if half of the observation days were missing, the number of observations would be roughly halved, but the area coverage could still be close to 80% if the remaining half of the days covered the Earth evenly. The vertical column sensitivity of the XCO_2 observations is shown in Figure 3D. It is close to one in the lower troposphere and then reduces gradually with altitude, maintaining a value of 0.5 in the lower stratosphere. With a strong sensitivity in the troposphere where significant XCO_2 signals occur due to surface emissions and removal of CO_2, OCO-2 effectively observes the atmosphere in the vertical domain.

3.3 MIP transport model run

The OCO-2 Model Intercomparison Project (MIP), organized by the OCO-2 Science Team, is a collaborative effort among atmospheric CO_2 modelers aiming to study the impact of assimilating OCO-2 retrieval data into atmospheric inversion models (Crowell et al., 2019; Peiro et al., 2022; Byrne et al., 2023). The project's primary objective is to generate an ensemble of CO_2 surface flux estimates to understand how these estimates, using OCO-2 retrievals and in situ measurements, depend on factors such as transport, data assimilation methodology, prior flux, and associated errors, and potential systematic errors in OCO-2 retrievals (across viewing modes like ocean glint, land nadir, and land glint). In the most recent version of the MIP (v10, Byrne et al., 2023), modelers used NASA's operational bias-corrected OCO-2 L2 Lite XCO_2 product v10 (Kiel et al., 2019) aggregated into 10-second averages. In situ data were sourced primarily from GlobalView-plus v6.1 (Schuldt et al., 2021). The submitted flux estimates cover from January 2015 to December 2020. Fossil fuel emissions were standardized using a temporally downscaled and extended dataset (Basu and Nassar, 2021) that was based on the ODIAC2019 dataset (Oda et al., 2018), while other prior flux estimates were independently selected by each modeling group.

3.4 Observing System Simulation Experiments (OSSEs)

Observing System Simulation Experiments (OSSEs) are a widely used research tool for evaluating the effectiveness of atmospheric observing systems, such as satellites, in situ measurement platforms, or data processing methods (Basu et al., 2018; Pandey et al., 2015). In this study, we utilize results from 10 modeling groups participating in the v10 MIP, listed in Table 1.

We use the posterior (final iteration of variational inversions) forward transport run of inversions assimilating point observations (in situ/IS inversions) over land and ocean. Within our OSSE setup, each MIP posterior model run is treated as an end-to-end simulation of atmospheric transport and CO_2 observing systems. The posterior fluxes of these model runs serve as the pseudo-truth. The 10s XCO_2 and in situ co-samples from the posterior CO_2 concentration fields of the model runs serve as synthetic observations. These co-samples are generated at the location and time of all in situ and satellite

observations. The satellite co-sample generation process uses the averaging kernel and the prior profile employed in the OCO-2 10s XCO_2 observations. Synthetic growth rate estimates are generated using the NOAA method on MBL point co-samples and the GRESO method on 10s XCO_2 co-samples.

390

Table 1 Specifications of OCO-2 MIP version 10 models used in this study[&].

MIP modelling group	Atmospheric transport model	Meteorology data	Transport model resolution (latitude × longitude)	Optimization method
AMES	GEOS-Chem	MERRA-2	4° × 5°	4D-Var
BAKER	PCTM	MERRA-2	4° × 5°	4D-Var
CAMS	LMDz	ERA5	1.9° × 3.75°	Variational
CMS-Flux	GEOS-Chem	MERRA-2	4° × 5°	4D-Var
COLA	GEOS-Chem	MERRA-2	4° × 5°	EnKF
CT	TM5	ERA-interm	2° × 3° *	EnKF
OU	TM5	ERA-interm	4° × 6°	4D-Var
TM5-4DVAR	TM5	ERA-interm	2° × 3°	4D-Var
UT	GEOS-Chem	GEOS-FP	4° × 5°	4D-var
WOMBAT	GEOS-Chem	MERRA-2	2° × 2.5°	Synthesis with MCMC

[&]Detailed description in Byrne et al. (2023) and Peiro et al. (2022) and NOAA MIP webpage (https://gml.noaa.gov/ccgg/OCO2_v10mip/ last access: 14-09-2023)

*1° × 1° over North America

395

Our pseudo-truth growth rates represent the net of the respective MIP runs' posterior fluxes. The MIP posterior fluxes are reported as 1° by 1° monthly components for ocean, land, and fossil categories. These components are combined globally to create a global monthly flux time series. The flux time series is then modeled as the sum of polynomial, harmonic, and residual terms (Equation 4). Combining the polynomial and residual terms creates a de-seasonalized monthly flux time
400 series, representing the de-seasonalized growth rate during a given month. The pseudo growth rate time series is then estimated from the de-seasonalized flux time series using the 2.124 PgC ppm^{-1} conversion factor (Ballantyne et al., 2012).

We evaluate the performance of the NOAA and GRESO methods at monthly and annual scales by calculating the correlation coefficient (R) and root mean square error (RMSE) compared to the pseudo truth. The RMSE quantifies the error relative to
405 the truth (i.e., the quadrature sum of accuracy against pseudo truth and precision), whereas R indicates the prediction

capability of the growth rates. For the synthetic growth rate estimates, we use a 0.1 ppm 1-standard-deviation error on individual NOAA in situ flask co-samples. For satellite growth rate errors, we propagate OCO-2 10s XCO_2 retrieval errors through the GRESO method.

To implement the NOAA growth rate method, we utilize the Python version of the NOAA DEI code. To ensure consistency with the data filtering and configuration implemented by NOAA, we tested our NOAA method implementation by reproducing the NOAA-reported growth rates using the site-wise observation file for our period of interest, 2015-2019. We found excellent agreement between the NOAA-reported annual growth rates and our own estimates (R = 1.0 and RMSE = 0.03 ppm $year^{-1}$).

OCO-2 co-samples from the MIP posteriors transport model are available until March 2021, enabling the calculation of 2020 annual growth rates. However, in situ co-samples provided by MIP ended in late 2020, preventing us from estimating 2020 growth rates. For consistency in our OSSE comparison between NOAA and OCO-2 data, our analysis is limited to the 2015–2019 period.

To use realistic growth rate variations in our OSSE, we use optimized posterior fluxes from real-world data. OSSE results with unrealistic growth rate variations could be misleading; for example, including an unrealistic annual growth rate of 10 ppm in our OSSE might lead to a significantly larger RMSE than what would be expected from the 2-3 ppm $year^{-1}$ growth rate range during 2015-2019. Conversely, a near-flat growth rate of 2 ppm $year^{-1}$ could result in an unrealistically large correlation range due to insufficient signal, i.e., growth rate variability. Fortunately, our study period includes a strong El Niño year 2015 (with a high growth rate of 3 ppm $year^{-1}$) and a weak La Niña year 2017 (with a growth rate of 2 ppm $year^{-1}$), allowing for a robust evaluation of the GRESO and NOAA methods at a range of growth rates.

4 Results and Discussion

We first present and discuss the results of our OSSEs. Utilizing the OSSEs, we conduct additional tests to evaluate the robustness of the GRESO method against changes in data density and gaps (Section 4.2). Subsequently, we briefly discuss some alternative methods for growth rate estimation (Section 4.3). We then present the real-world measured CO_2 growth rates (Section 4.4). Following this, we discuss the expected latency in growth rates for the NOAA and GRESO methods (Section 4.5).

4.1 OSSE results

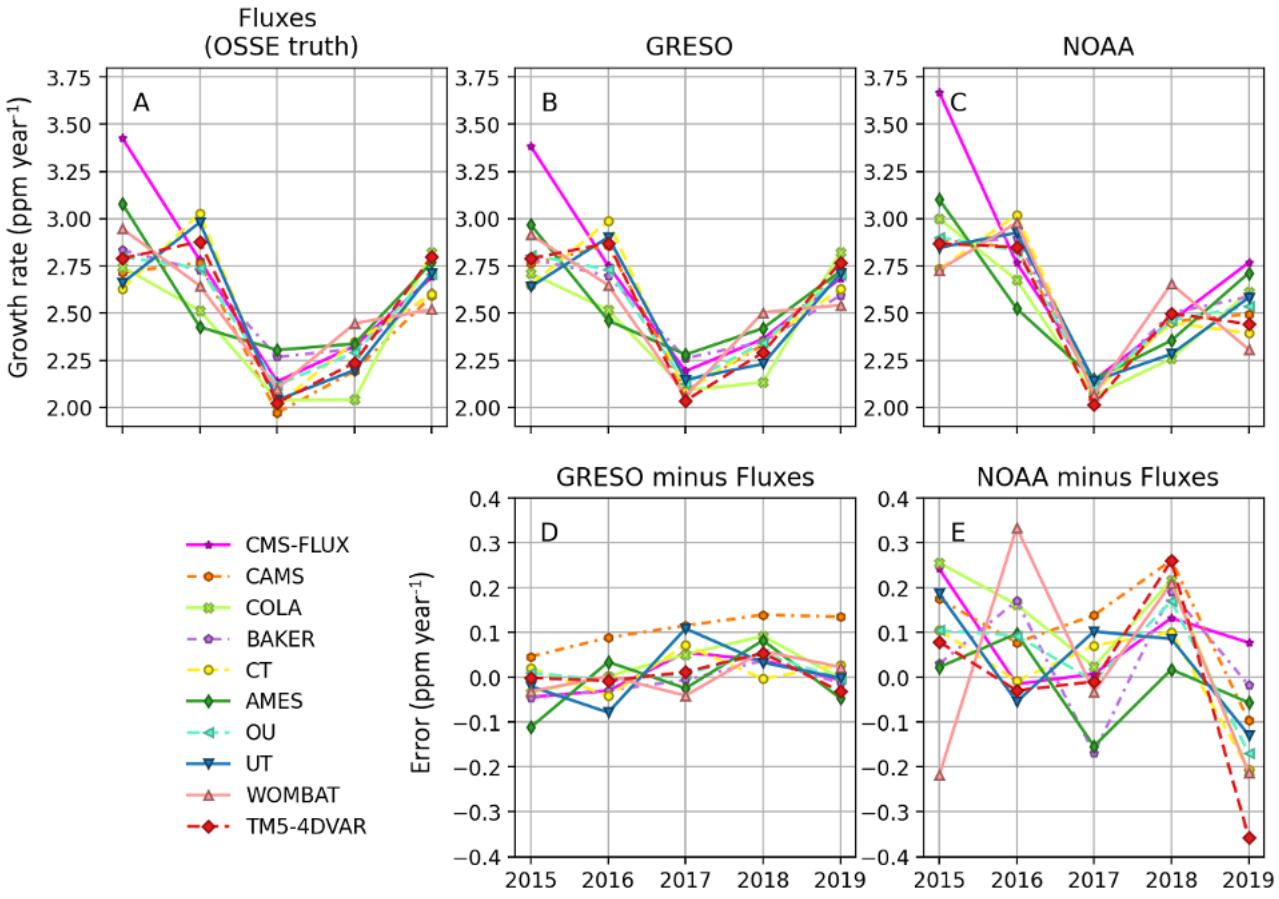

Figure 5. CO_2 growth rate estimates on annual scale. Panel (A) presents the flux-based growth rate estimates, considered the OSSE truth, across various MIP models. Panels (B) and (D) display the annual growth rate estimates generated by the GRESO method and their deviations from the OSSE truth, respectively. Similarly, Panels (C) and (E) depict the annual growth rate estimates and deviations from the truth for the NOAA method. The GRESO and NOAA methods calculate growth rates using the OCO-2 data and MBL in situ co-samples, respectively, which are derived from the mole fraction fields of MIP models.

Figure 5 shows the estimated annual growth rates and the corresponding OSSE truths, i.e., flux-based growth rates, for the 10 MIP transport model runs. The performance of the growth rate methods for a given MIP model is evaluated with RMSE and R of the truth and estimates (Figure 6). The differences in these evaluation metrics for various MIP models result from the interplay of differences in atmospheric transport and spatial and temporal distribution of truth fluxes. For instance, a flux anomaly will appear more pronounced in an in situ network if the atmospheric transport of the model efficiently conveys the flux signal to the network's location. Conversely, if the anomaly signal is positioned to be carried away from the network by the transport, the opposite effect can occur. The overall performance of the growth rate methods is assessed by taking the

median of the 10 RMSE and R values, which are presented in Table 2. On the annual scale, the GRESO method exhibits strong performance with a median R of 0.997 and a median RMSE of 0.04 ppm $year^{-1}$. The NOAA method has a median R of 0.93 and RMSE of 0.12 ppm $year^{-1}$. Despite relying on a limited number of MBL sites, the NOAA method demonstrates an impressive skill in estimating annual growth rates.

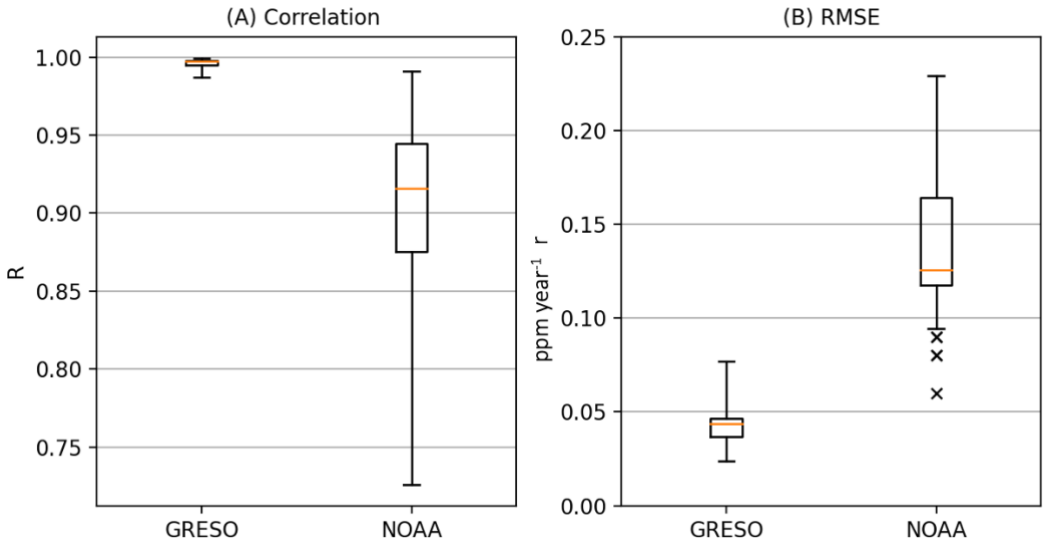

Figure 6. Comparative performance of growth rate methods on annual scale. The GRESO method employs OCO-2 satellite data for sampling, while NOAA utilizes in situ MBL observations. Panel (A) shows the correlation coefficients (R), and Panel (B) presents the RMSE associated with annual growth rates. In each box-and-whisker plot, the orange horizontal line represents the median value. The boxes delineate the interquartile range, and the whiskers extend to the full range of correlation coefficients and RMSE values obtained across the ten MIP model runs in the OSSE. Black crosses indicate the random error (i.e., without bias) in annual growth rates reported by NOAA for 2015-2019. Note that two pairs of years have nearly identical growth rate uncertainties, resulting in only three visible crosses.

Table 2. Evaluation metrics for data-driven growth rate estimates[&].

Growth rate method	Annual		Monthly		5 Years
	R	RMSE (ppm $year^{-1}$)	R	RMSE (ppm $year^{-1}$)	RMSE (ppm $year^{-1}$)
NOAA	0.93	0.12	0.47	1.26	0.033
GRESO	1.0	0.04	0.77	0.75	0.016

[&]The table presents the median values of R and RMSE between estimated and pseudo growth rates across 10 MIP transport model runs.

Figure 7 and Table 2 present the results for monthly scale. Note that the methods are evaluated after removing the mean seasonal cycle from the truth flux and growth rate time series. The GRESO method demonstrates a median R of 0.77 and median RMSE of 0.75 ppm $year^{-1}$ (~0.06 ppm $month^{-1}$), whereas the NOAA method has a lower median R of 0.47 and a higher median RMSE of 1.26 ppm $year^{-1}$ (0.11 ppm $month^{-1}$). On 5-year scale (Table 2), we calculate median RMSE (equivalent to the mean absolute difference) as 0.016 ppm $year^{-1}$ for the GRESO method and 0.033 ppm $year^{-1}$ for the NOAA method. The NOAA method after 5 years has very low uncertainty which most likely reflects the nearly complete atmospheric mixing of flux anomalies (including into most of the upper atmosphere) after such a long period. Note that the sampling error estimates from our OSSE tests are expected to be less robust for monthly and 5-year errors in comparison to that of annual estimates. This is due to the limited number of data points for 5-year scales (one per model), and the monthly resolution of fluxes in the MIP models does not account for highly transient emissions events.

We find the NOAA annual growth rate sampling error to be 0.12 ppm $year^{-1}$. The sampling error originates from two primary sources: (1) Variations in the Marine Boundary Layer (MBL) network, including site additions or removals and temporal data gaps (Lan et al., 2023) (see Figure 2); and (2) The inherent uncertainty involved in approximating the true, mass-weighted, three-dimensional average CO_2 concentration for the entire atmosphere using surface network data. Additional non-sampling errors not captured in the OSSE include (1) the long-term reproducibility of reference gas standards, with a 1-standard-deviation uncertainty of approximately 0.03 ppm dating back to the 1980s (0.01 ppm with a new reference system introduced in 2017), and (2) transient, unexplained systematic analytical errors.

The total error in the NOAA growth rates would be derived by summing the sampling and non-sampling errors in quadrature. The non-sampling errors are expected to largely cancel out during the growth rate calculation, making their contribution to the total error negligible compared to the dominant sampling error of 0.12 ppm $year^{-1}$. NOAA-reported growth-rate errors of 0.06-0.09 ppm $year^{-1}$ (Figure 6) account for changes in the surface network over time (horizontal sampling error) and small, unexplained systematic analytical errors (non-sampling error).

Differences between the reported errors and our RMSE estimates for NOAA can be attributed to the fact that NOAA's uncertainty quantification method, in effect, only addresses the horizontal atmospheric sampling uncertainty with the bootstrapping method (Section 2.1). North-south interhemispheric mixing timescales are roughly one year, and east-west mixing timescales are weeks, which means that flux anomalies cannot "hide" from the MBL sites for very long. In contrast, troposphere-stratosphere mixing timescales typically take several years (~2.5 years). Model simulations and aircraft profiles indicate rather homogeneous vertical profiles of CO_2 above remote locations within the troposphere, suggesting that the key difference between the MBL and total column estimates relates to the estimation of dispersion of flux anomalies into the stratosphere. These signals are not considered in NOAA's uncertainty estimates, which are primarily derived using bootstrapping methods that address the uncertainty related to surface-horizontal sensitivity to flux anomalies. However, we

can estimate the vertical error component (σ_v) in the NOAA method using the horizontal uncertainty (σ_h ~ 0.08; median of black crosses) with the OSSE-estimated total uncertainties (σ_{total} ~ 0.12; orange lines) shown in Fig. 6B. Assuming that NOAA's uncertainty quantification method gives a good estimate of the σ_h and $\sigma_{total}^2 = \sigma_h^2 + \sigma_v^2$, we estimate σ_v = 0.09 ppm year^{-1}. This suggests the unaccounted vertical component of the uncertainty is roughly equal to the reported horizontal uncertainty.

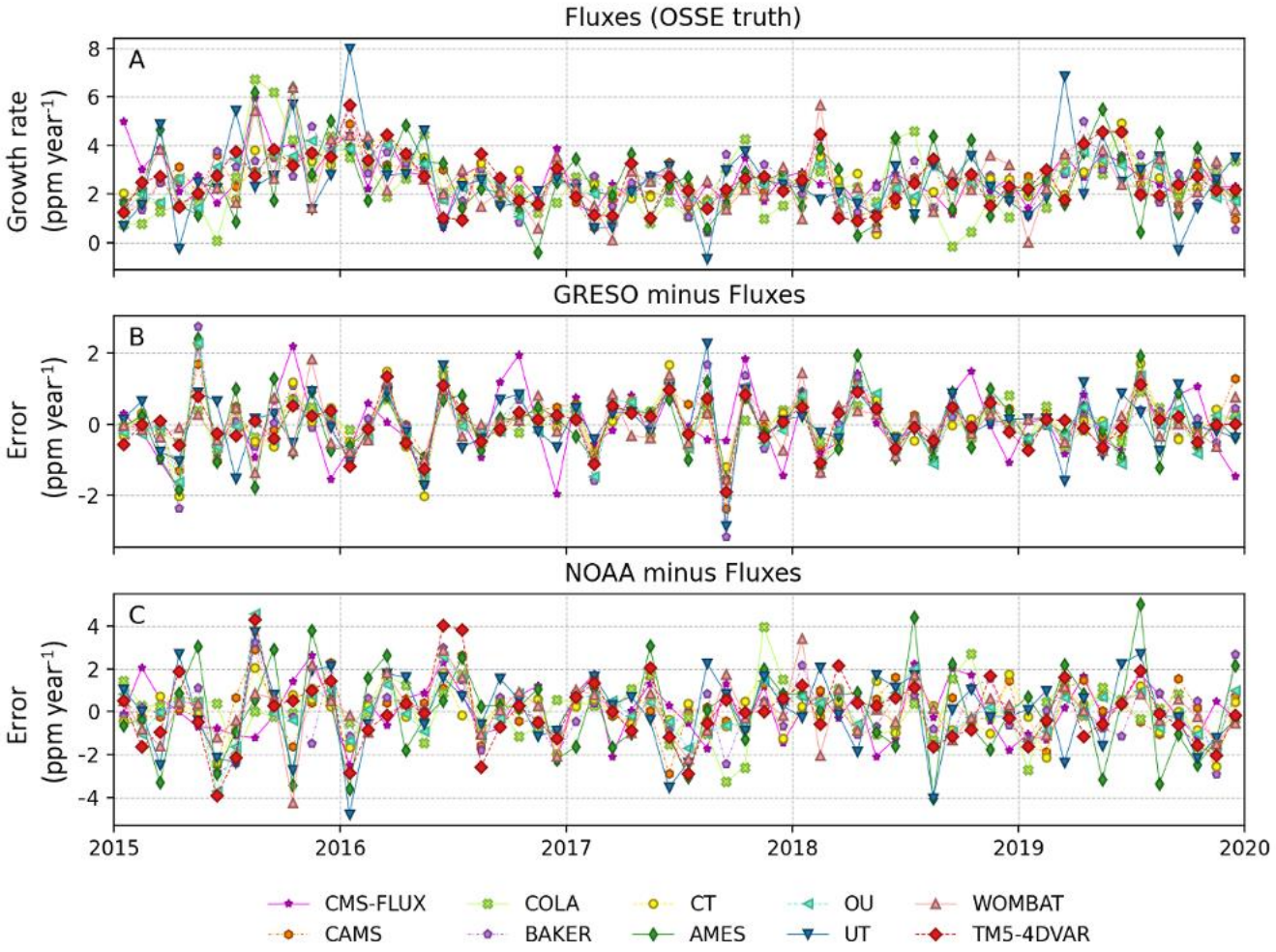

Figure 7. Performance of growth rate methods on monthly scale. Panel (A) displays flux-based deseasonalized growth rate estimates across various MIP models, treated as the OSSE truth. Panels (B) and (C) depict the discrepancies in growth rates as determined by the GRESO and NOAA methods, respectively. The y-axis range of Panel (B) is roughly half that of Panel (C), highlighting the smaller errors in the GRESO method compared to the NOAA method. The median monthly growth rate RMSE and R for the methods are given in Table 2.

Overall, across various temporal scales, the GRESO method outperforms the NOAA method in terms of whole-atmosphere sampling errors, largely due to its enhanced horizontal and vertical sampling capabilities provided by satellite observations. On an annual scale, GRESO's RMSE is three times lower than NOAA's. On monthly and 5-year scales, its RMSE is half that of NOAA's. Note that these RMSE values represent only the whole-atmosphere sampling errors, including the effect of change in coverage of high-quality OCO-2 data due to clouds and aerosols. The real-world errors in satellite growth rates are expected to be dominated by systematic biases in satellite data.

4.2 Robustness of GRESO method

The GRESO method has been developed based on existing growth rate estimation techniques, such as the NOAA method, but with refinements based on end-to-end OSSE transport model runs to optimally leverage satellite sampling of the atmosphere. The final version of the GRESO method presented here achieves optimal alignment between estimated growth rates and their corresponding pseudo truths, which represent the global net of fluxes. Alternative methods for growth rate estimation from satellite data have been proposed in other studies (Buchwitz et al., 2018). Table 3 provides evaluations of alterations made to the method's settings, such as the utilization of different temporal and spatial bins, to elucidate their influence on the method's efficacy in growth rate estimations. Buchwitz et al. (2018) employed 10° by 10° spatial bins and monthly temporal bins, coupled with direct global averaging. In contrast, the GRESO method employs 5° by 5° spatial bins and 16-day temporal bins, and a two-step averaging process: first along latitude bands and subsequently along longitudes. Our tests indicate that the performance of the GRESO method diminishes slightly when we adopt the settings used by Buchwitz et al. (2018).

The sensitivity of the GRESO method to observation gaps, which satellites are prone to, is an important consideration for its utility. Our OSSE tests include the temporal and spatial gaps in the original OCO-2 dataset. These gaps include multi-day discontinuities and a substantial gap from July 31 to September 19, 2017. To further scrutinize the robustness of the GRESO method against observation gaps, we subjected it to stress tests involving artificial reductions in observation numbers. Table 4 presents the outcomes. The GRESO method performs well even when restricted to ocean-based ($R = 0.99$) or land-based ($R = 0.98$) observations. This implies that specialized satellites focusing solely on oceanic or terrestrial observations could yield accurate growth rate estimates. These findings are pertinent to estimating growth rates of CO_2 and methane using satellites that primarily observe over land such as GOSAT and TROPOMI (Buchwitz et al. 2018; Balasus et al., 2023; Lorente et al., 2021; O'Dell, et al., 2018; Schneising et al., 2019).

Table 3. Sensitivity analysis of the GRESO method for temporal and spatial bin sizes[&].

Method alterations	Annual		Monthly	
	R	RMSE (ppm year^{-1})	R	RMSE (ppm year^{-1})
GRESO method (original)*	0.997	0.041	0.802	0.732
Monthly temporal bins[a]	0.988	0.063	0.751	0.684
5-day temporal bins	0.985	0.069	0.707	0.888
Global spatial averaging [a]	0.987	0.065	0.697	0.900
10° by 10° spatial bins[a]	0.985	0.055	0.713	0.828

[&]The table presents the median values of R and RMSE between estimated and pseudo growth rates in the 10 MIP model runs. The base GRESO method is detailed in Figure 4. Values are rounded to three decimal places for precise comparisons.
*Original GRESO setup: 5° x 5° spatial bins and 16-day temporal bins.
[a] Settings used by Buchwitz et al. (2018)

We assess the GRESO method's performance under significantly reduced OCO-2 coverage conditions—50%, 10%, and 1% of the total 10s XCO_2 observations. Despite data limitations, the method maintains high accuracy for annual CO_2 growth rate estimates (R > 0.95). However, its performance suffers more noticeably at the monthly scale (R = 0.45 for 1% data), a decline that aligns with the NOAA method's performance based on limited in situ MBL observations. We also evaluated the impact of systematic omissions in data, specifically from the Sahara and Amazonia regions. These tests revealed that the GRESO method continues to perform robustly at both annual and monthly scales, albeit with a slight increase in the annual RMSE to 0.057 ppm year^{-1}.

The overall accuracy of GRESO growth rates hinges on the magnitudes of the GRESO method's sampling errors versus the systematic errors in XCO_2 measurements. This total error should be the quadrature sum of the two errors, assuming these error sources are independent. Our OSSEs show that the sampling error of the GRESO method is minimal. Therefore, the principal error source is systematic errors in XCO_2 observations. Fortunately, many of these biases exhibit low interannual variability, suggesting they might negate each other during growth rate calculations, leaving only temporally fluctuating biases to affect the GRESO method (Section 2). Evidence indicates the existence of time-varying biases in the Ocean Glint data from OCO-2. Research teams involved in the OCO-2 version 10 MIP have observed significant discrepancies between flux estimates derived from OCO-2's ocean glint inversions and those obtained from NOAA and land XCO_2 inversions. Assuming accurate initialization of the MIP inversions (spin-up), the variations in posterior fluxes from ocean inversions, compared to land data and NOAA inversions, point to potential growth rate biases in OCO-2 ocean glint data (refer to

Section 4.1 in Byrne et al., 2023 for more details). Additionally, validation studies utilizing data from the TCCON network support the presence of this growth rate bias in OCO-2 ocean glint observations (as illustrated in Figure 9D of Taylor et al., 2023). Such systematic growth rates errors will be the primary factor dictating the overall precision of real-world GRESO growth rates. Concurrently, substantial efforts are underway to identify and mitigate these systematic biases, with an expectation of continued improvement in the accuracy of satellite observations.

Table 4. The performance of the GRESO method with a hypothetical reduction in OCO-2 observation coverage[&].

Hypothetical coverage	**Annual**		**Monthly**	
	R	RMSE (ppm year^{-1})	R	RMSE (ppm year^{-1})
Ocean (OG)	0.990	0.049	0.691	0.828
Using Land observations (LNLG)	0.984	0.097	0.686	0.972
1 % OCO-2 observations	0.951	0.123	0.449	1.440
10 % OCO-2 observations	0.971	0.083	0.647	0.876
50 % OCO-2 observations	0.996	0.046	0.723	0.876
Sahara[1] seasonal[a] gap	0.992	0.057	0.784	0.732
Sahara[1] annual[b] gap	0.992	0.057	0.780	0.733
Amazonia[2] seasonal[a] gap	0.992	0.057	0.784	0.731
Amazonia[2] annual[b] gap	0.992	0.057	0.779	0.732

[&]The table presents the median values of R and RMSE between estimated and pseudo growth rates across 10 MIP model runs. Values are shown up to three decimal places for precise comparisons.
[1]Sahara region gap: -18° to 29° longitude and -2° to 37° latitude.
[2]Amazonia region gap: -79° to -67° longitude and -13° to -5° latitude.
[a]Seasonal gap: 1st January 2017 –1st April 2017
[b]Annual gap: 1st January 2017 –1st January 2018

4.3 Alternative growth rate methods

4.3.1 WMO WDCGG

The World Meteorological Organization (WMO) World Data Centre for Greenhouse Gases (WDCGG) also reports global CO_2 averages using methods similar to those of NOAA (Tsutsumi et al., 2009). However, WDCGG incorporates a more extensive dataset, sourced from various independent laboratories, including continental sites. This results in a higher mean CO_2 mole fraction and a greater amplitude of the seasonal cycle than those estimated by NOAA. Notably, neither method offers a comprehensive representation of the troposphere or stratosphere. Wu et al. (2024) have investigated the discrepancies between the growth rate estimates of NOAA and WMO and reported that the growth rate values from the two sources exhibit strong agreement.

4.3.2 GEOS/OCO-2

The GRESO method, leveraging its data-driven nature and utilization of level-2 OCO-2 XCO_2 data, offers computational efficiency in generating growth rate estimates. NASA's GEOS/OCO-2 model uses XCO_2 observations to constrain a 4-dimensional CO_2 mole fraction field, employing an intricate level-3 system for assimilating OCO-2 data (Weir et al., 2021; Weir et al., 2022). The GEOS/OCO-2 atmospheric carbon monitoring system updates global CO_2 concentrations at three-hour intervals by incorporating bias-corrected OCO-2 XCO_2 retrievals (version 10) via a statistical data assimilation technique. Such assimilation enables the GEOS method to harmonize its simulations with empirical observations, thereby adjusting the state of atmospheric CO_2 to align closely with observed values. The growth rate values are readily calculated by averaging the optimized CO_2 mole fraction field.

4.4 Measured growth rates

Figure 8 shows real-world growth rate estimates for 2015–2020 derived from OCO-2 data via the GRESO method, NOAA-reported estimates (Lan et al., 2023), and growth rates from the GEOS/OCO-2 level-3 product. Table 5 encapsulates the correlation coefficients (R) and root mean square difference (RMSD) between each pair of estimates. Over the 6-year span, annual growth rates from GRESO and NOAA estimates align well, achieving an R of 0.94 and an RMSD of 0.13 ppm $year^{-1}$ for annual growth rates. Given the associated sampling errors in these methods, this level of agreement is expected. GEOS/OCO-2 also shows good agreement with both NOAA and GRESO. Since GEOS/OCO-2 uses the NOAA MBL growth rate for prior information, its alignment in between GRESO and NOAA values is foreseeable. The mean growth rate over the six years for NOAA and GRESO agree very well with less than 0.03 ppm $year^{-1}$. This is also expected, given the mitigation of sampling errors resulting from the vertical and horizontal mixing over the span of 6 years (Section 4.1).

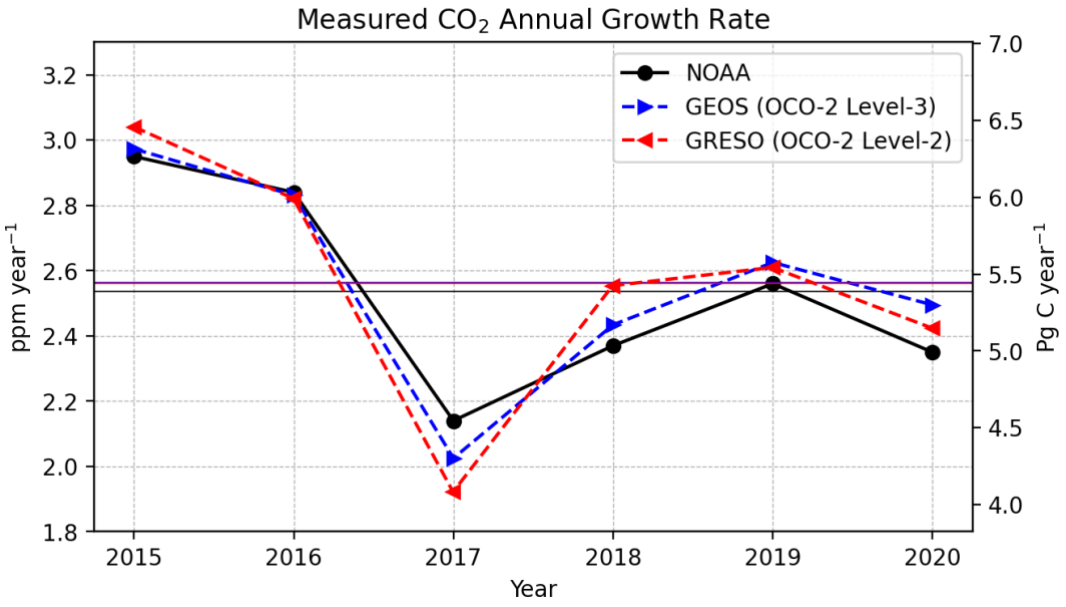

Figure 8. Real-world CO_2 growth rates estimates from (1) the NOAA method based on MBL in situ observations, (2) the GRESO OCO-2 level-2 method, and (3) the GEOS/OCO-2 level-3 product. The horizontal lines (overlapping GRESO and GEOS) represent the mean growth rate in 2015-2020.

Table 5. Comparison of measured growth rates for 2015-2020[&].

Method pairs	Annual R	Annual RMSD (ppm year^{-1})	6-year Mean Difference (ppm year^{-1})
GRESO-NOAA	0.92	0.13	0.027
GEOS- NOAA	0.97	0.08	0.029
GRESO-GEOS	0.98	0.08	–0.002

[&]Root mean square difference (RMSD) and Pearson correlation coefficients (R) are shown. NOAA uses MBL in situ observations GEOS (level-3) and GRESO (level-2) growth rate methods use OCO-2 version 10 observations.

Taylor et al. (2023) presented estimates of real-world growth rates using OCO-2 data, drawing on the methodology outlined by Buchwitz et al. (2018). They compared these rates with those derived from NOAA and found a strong correlation with NOAA's annual growth rates (R = 0.98), exceeding the NOAA correlation with GRESO (R = 0.92). The main reason for the stronger alignment is that both Buchwitz et al. (2018) and NOAA growth rate methods generate a smoothed version of the annual growth rates. The Buchwitz et al. (2018) method gives a 6-month smoothed version of the annual growth rate time series and therefore does not capture the exact atmospheric mass change of CO_2 over the course of a year. The smoothing in the NOAA method is attributable to a combination of limited marine boundary layer sampling, and the filtering and

averaging methods employed. Consequently, the method of Buchwitz et al. (2018) strongly agrees with NOAA. Smoothing the GRESO growth rates would similarly enhance its correlation with NOAA, as evidenced in Figure 8. However, such a modification would compromise the GRESO method's objective to estimate the atmospheric CO_2 mass change over the course of an exact period, like a year.

4.5 Latency in the availability of growth rates

NOAA growth rate estimates of a year may undergo multiple revisions over several following months until it finally converges. This latency in convergence in growth rates from NOAA MBL samples and their subsequent revision can be primarily ascribed to two factors: First, the logistics associated with transporting weekly flask air samples from remote MBL locations to the NOAA laboratory in Boulder, Colorado, often entail a delay of months. Second, the utilization of the CCGCRV algorithm (Section 2.2) is sensitive to the temporal coverage of data, and edge effects can cause incremental estimates to change as more data are added to one end. The availability NOAA MBL-based growth rate estimates has a latency of about four months. Earlier growth rate estimates are not deemed reliable by NOAA due to large uncertainty.

We illustrate the NOAA growth rate latency by performing the following experiment. For each year between 2014 and 2021, we calculate the CO_2 growth rate using NOAA's DEI procedure based on MBL data available *M* months after the year ended. Figure 9 shows the growth rates estimated for each year as a function of *M*, compared to the final value (largest possible *M* for each year). While NOAA estimates typically stabilize within four months, the convergence period for certain years can extend beyond. Friedlingstein et al. (2022b) reported the 2019 CO_2 growth rate to be 2.56 ppm $year^{-1}$, based on an access date of 25 September 2022. A more recent update calculates the 2019 growth rate as 2.50 ± 0.06 ppm $year^{-1}$ (Lan et al., 2023; accessed on 2 October 2023). While this is a less than 1 standard deviation uncertainty change, it happened three years after the fact. In general, such changes due to re-calculation are more pronounced closer to the calendar year in question.

Growth rates estimated by the GRESO method have a much shorter convergence period. By leveraging the more spatially extensive atmospheric sampling capabilities of satellite observations, GRESO forgoes NOAA's approach of curve fitting and frequency domain filtering to mitigate noise, so the GRESO method is generally not subject to curve fitting end effects. Linear interpolation of the residuals is utilized on the global representative CO_2 time series to bridge any data gaps. The primary limitation of GRESO convergence is its 3-point median step (Figure 4). Hence, the method attains stability once it gathers two 16-day global representative CO_2 data points after midnight on December 31 of a year, implying convergence by the end of the subsequent January if OCO-2 data are available immediately. It is important to note that even though the GRESO method reaches convergence within a month, changes in the growth rate values may still occur subsequently. This is

because the satellite observation values may undergo changes due to improvements made in retrieval algorithms, calibration, and other factors (Taylor et al., 2023).

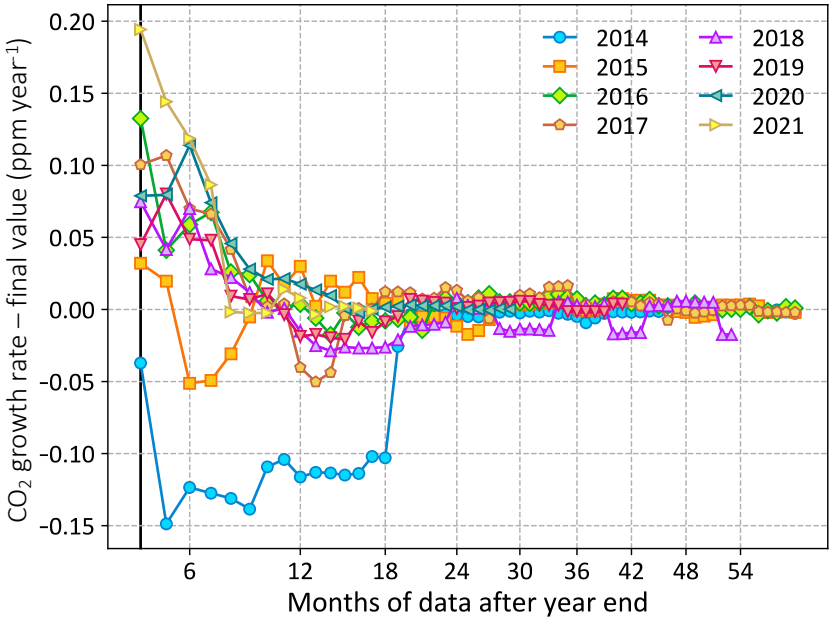

Figure 9. The convergence of annual CO_2 growth rates is estimated as a function of months beyond each year. The vertical black line marks a four-month lag when NOAA first publishes growth rate for a year. The difference (Y-axis) between final growth rates and the values estimated using observations available in the months following each year-end (X-axis) is shown. This difference indicates an error in the NOAA estimate attributable to the time required for the estimates to stabilize.

GEOS/OCO-2 further amplifies the ability to deduce growth rates with minimal delay, attributed to its assimilation of the available OCO-2 data. However, GEOS/OCO-2 stands as an advanced assimilation system necessitating input surface fluxes, meteorology, and high-end computing resources. The GRESO method presented in this study, on the other hand, can deliver growth rate predictions within seconds following the availability of OCO-2 data. Although the preliminary stream of OCO-2 data is accessible after a one-week delay, better-quality operational data is typically available after a month's wait. Overall, considering both the delay in OCO-2 data availability and methodological constraints, a practical convergence period of up to two months is expected for GRESO and GEOS/OCO-2.

5 Summary and outlook

In this study, we have introduced the GRESO method, a robust method for calculating CO_2 growth rates and global means utilizing satellite observations. We employed an OSSE framework involving multiple transport models to evaluate the

atmospheric sampling errors associated with the GRESO and the NOAA MBL-based DEI methods, where the latter relies on MBL in situ data. Our assessments were benchmarked against flux-based CO_2 growth rates tracking the true CO_2 growth in the OSSEs.

Our findings demonstrate that the NOAA method utilizing MBL in situ data performs very well on an annual scale despite its limited surface sampling. However, whole-atmosphere sampling error for NOAA's annual growth rate predictions exceeds the uncertainty estimates from NOAA's bootstrapping analysis of real data. This discrepancy suggests an additional error source, likely stemming from restricted vertical sensitivity. Over five-year spans, however, the NOAA method's errors are remarkably low. This aligns with the observation that over a five-year duration, any instantaneous flux anomaly would become extensively mixed throughout most of the atmosphere, a phenomenon less pronounced over a single year and more limited to the troposphere.

At annual time scales, the GRESO method utilizing OCO-2 data has sampling errors that are two to three times lower than the NOAA DEI approach. Our OSSE analysis suggests that if systematic errors in satellite observations are sufficiently mitigated, OCO-2's atmospheric sampling can provide reliable growth rate estimates at short periods like a month or season. It is expected that advances in retrieval methodologies and enhanced bias correction techniques, such as using machine learning algorithms (Balasus et al., 2023), will mitigate systematic errors in satellite data, facilitating accurate and promptly available growth rate estimates. However, as shown in Figure 8, even with the current level of biases, OCO-2 version 10 data with GRESO provides reasonable real-world growth rate estimates.

Stress tests on the GRESO method, incorporating reductions in observation counts and introducing spatial gaps, affirmed its resilience and accuracy under suboptimal conditions. GRESO could reliably estimate growth rates using solely land- or ocean-based observations. This adaptability is particularly relevant for methane growth rate calculations using TROPOMI and other CO_2 and methane satellites that predominantly observe over land.

Looking forward, we anticipate that satellites will complement the long CO_2 record from in situ networks with accurate, low-latency growth rate estimates on shorter timescales. However, the growth rate estimates from long-term in situ observations from NOAA will be critically needed (Houweling et al., 2012). In situ sites from the NOAA network, such as Mauna Loa and American Samoa, provide invaluable data, serving as a priori CO_2 information for satellites like OCO-2 and the TCCON network. For confidence to grow in GRESO and similar satellite-based methods, their continued comparison with purely in situ-based approaches, such as NOAA’s DEI method, will be required for the foreseeable future. The enduring in situ atmospheric CO_2 record, initiated by Dave Keeling's seminal work at the Mauna Loa Observatory (Keeling, 1960), has been an indispensable asset. For over half a century, it has continuously provided insights into the 'small but persistent growth,' enhancing our understanding of anthropogenic impacts on the Earth's climate.

Data Availability: The OCO XCO_2 data are publicly available at the NASA Goddard Earth Science Data and Information Services Center (GES-DISC). The Lite files, which include the quality-flagged and bias-corrected estimates of XCO_2, can be obtained at https://doi.org/10.5067/E4E140XDMPO2 (OCO Science Team., 2020). Level-3 GEOS XCO_2 data are available at https://doi.org/10.5067/Y9M4NM9MPCGH (Weir et al., 2022). The fluxes and in situ and satellite co-samples of the MIP model runs are available at the NOAA MIP webpage (https://gml.noaa.gov/ccgg/OCO2_v10mip/ last access: 14 September 2023). NOAA CO_2 samples and growth rate values are available at https://gml.noaa.gov/ccgg/ last access: 14 September 2023).

Acknowledgements: Part of this work was carried out at the Jet Propulsion Laboratory, California Institute of Technology, under contract to the National Aeronautics and Space Administration (80NM0018D0004). The authors thank Dr. Vivienne Payne, project scientist of OCO-2 mission, for her feedback.

References

Bacastow, R. B. (1976). Modulation of atmospheric carbon dioxide by the Southern Oscillation. Nature, 261(5556). https://doi.org/10.1038/261116a0

Ballantyne, A. P., Alden, C. B., Miller, J. B., Tans, P. P., and White, J. W. C.: Increase in observed net carbon dioxide uptake by land and oceans during the past 50 years, Nature, 488, 70–72, https://doi.org/10.1038/nature11299, 2012.

Baker, D. F., Bell, E., Davis, K. J., Campbell, J. F., Lin, B., and Dobler, J.: A new exponentially decaying error correlation model for assimilating OCO-2 column-average CO2 data using a length scale computed from airborne lidar measurements, Geosci. Model Dev., 15, 649–668, https://doi.org/10.5194/gmd- 15-649-2022, 2022.

Barkhordarian, A., Bowman, K. W., Cressie, N., Jewell, J., and Liu, J.: Emergent constraints on tropical atmospheric aridity - Carbon feedbacks and the future of carbon sequestration, Environ. Res. Lett., 16, https://doi.org/10.1088/1748-9326/ac2ce8, 2021.

Basu, S. and Nassar, R.: Fossil Fuel CO_2 Emissions for the OCO2 Model Intercomparison Project (MIP) (2020.1), Zenodo [data set], https://doi.org/10.5281/zenodo.4776925, 2021

Basu, S., Baker, D. F., Chevallier, F., Patra, P. K., Liu, J., and Miller, J. B.: The impact of transport model differences on CO2 surface flux estimates from OCO-2 retrievals of column average CO2, Atmos. Chem. Phys., 18, 7189–7215, https://doi.org/10.5194/acp-18-7189-2018, 2018.

Bennedsen, M., Hillebrand, E., & Koopman, S. J. (2023). On the evidence of a trend in the CO2 airborne fraction. *Nature*, *616*(7956), E1-E3. https://doi.org/10.1038/s41586-023-05871-6

Balasus, N., Jacob, D. J., Lorente, A., Maasakkers, J. D., Parker, R. J., Boesch, H., Chen, Z., Kelp, M. M., Nesser, H., and Varon, D. J.: A blended TROPOMI+GOSAT satellite data product for atmospheric methane using machine learning to correct retrieval biases, Atmos. Meas. Tech., 16, 3787–3807, https://doi.org/10.5194/amt-16-3787-2023, 2023.

Buchwitz, M., Reuter, M., Schneising, O., Noël, S., Gier, B., Bovensmann, H., Burrows, J. P., Boesch, H., Anand, J., Parker, R. J., Somkuti, P., Detmers, R. G., Hasekamp, O. P., Aben, I., Butz, A., Kuze, A., Suto, H., Yoshida, Y., Crisp, D., and O'Dell, C.: Computation and analysis of atmospheric carbon dioxide annual mean growth rates from satellite observations during 2003-2016, Atmos. Chem. Phys., 18, 17355–17370, https://doi.org/10.5194/acp-18-17355-2018, 2018.

Byrne, B., Baker, D. F., Basu, S., Bertolacci, M., Bowman, K. W., Carroll, D., Chatterjee, A., Chevallier, F., Ciais, P., Cressie, N., Crisp, D., Crowell, S., Deng, F., Deng, Z., Deutscher, N. M., Dubey, M. K., Feng, S., García, O. E., Griffith, D. W. T., Herkommer, B., Hu, L., Jacobson, A. R., Janardanan, R., Jeong, S., Johnson, M. S., Jones, D. B. A., Kivi, R., Liu, J., Liu, Z., Maksyutov, S., Miller, J. B., Miller, S. M., Morino, I., Notholt, J., Oda, T., O'Dell, C. W., Oh, Y. S., Ohyama, H., Patra, P. K., Peiro, H., Petri, C., Philip, S., Pollard, D. F., Poulter, B., Remaud, M., Schuh, A., Sha, M. K., Shiomi, K., Strong, K., Sweeney, C., Té, Y., Tian, H., Velazco, V. A., Vrekoussis, M., Warneke, T., Worden, J. R., Wunch, D., Yao, Y., Yun, J., Zammit-Mangion, A., and Zeng, N.: National CO2 budgets (2015-2020) inferred from atmospheric CO2 observations in support of the global stocktake, Earth Syst. Sci. Data, 15, 963–1004, https://doi.org/10.5194/essd-15-963-2023, 2023.

Byrne, B., Bowman, K., Pascolini-campbell, M., Pandey, S., Miyazaki, K., van der Werf, G. R., Wunch, D., Wennberg, P. O., Roehl, C. M., and Sinha, S.: Unprecedented Canadian forest fire carbon emissions during 2023, Res. Sq. Prepr., https://doi.org/https://doi.org/10.21203/rs.3.rs-3684305/v1, 2023.

CCGCRV code, NOAA: Curve Fitting Methods Applied to Time Series in NOAA/GML available at https://gml.noaa.gov/ccgg/mbl/crvfit/crvfit.html; last access 15 November 2023.

Chatterjee, A., Gierach, M. M., Sutton, A. J., Feely, R. A., Crisp, D., Eldering, A., Gunson, M. R., O'Dell, C. W., Stephens, B. B., and Schimel, D. S.: Influence of El Niño on atmospheric CO2 over the tropical Pacific Ocean: Findings from NASA's OCO-2 mission, Science (80)., 358, https://doi.org/10.1126/science.aam5776, 2017.

Conway, T. J., Tans, P. P., Waterman, L. S., Thoning, K. W., Kitzis, D. R., Masarie, K. A., and Zhang, N.: Evidence for interannual variability of the carbon cycle from the National Oceanic and Atmospheric Administration/Climate Monitoring and Diagnos- tics Laboratory Global Air Sampling Network, J. Geophys. Res.- Atmos., 99, 22831–22855, https://doi.org/10.1029/94JD01951, 1994.

Cox, P. M., Pearson, D., Booth, B. B., Friedlingstein, P., Huntingford, C., Jones, C. D., and Luke, C. M.: Sensitivity of tropical carbon to climate change constrained by carbon dioxide variability, Nature, 494, 341–344, https://doi.org/10.1038/nature11882, 2013.

Crisp, D., Pollock, H. R., Rosenberg, R., Chapsky, L., Lee, R. A. M., Oyafuso, F. A., Frankenberg, C., O'Dell, C. W., Bruegge, C. J., Doran, G. B., Eldering, A., Fisher, B. M., Fu, D., Gunson, M. R., Mandrake, L., Osterman, G. B., Schwandner, F. M., Sun, K., Taylor, T. E., Wennberg, P. O., and Wunch, D.: The on-orbit performance of the Orbiting Carbon Observatory-2 (OCO-2) instrument and its radiometrically calibrated products, Atmos. Meas. Tech., 10, 59–81, https://doi.org/10.5194/amt-10-59-2017, 2017.

Crowell, S., Baker, D., Schuh, A., Basu, S., Jacobson, A. R., Cheval- lier, F., Liu, J., Deng, F., Feng, L., McKain, K., Chatterjee, A., Miller, J. B., Stephens, B. B., Eldering, A., Crisp, D., Schimel, D., Nassar, R., O'Dell, C. W., Oda, T., Sweeney, C., Palmer, P. I., and Jones, D. B. A.: The 2015–2016 carbon cycle as seen from OCO-2 and the global in situ network, Atmos. Chem. Phys., 19, 9797–9831, https://doi.org/10.5194/acp-19-9797-2019, 2019.

Eldering, A., Wennberg, P. O., Crisp, D., Schimel, D. S., Gunson, M. R., Chatterjee, A., Liu, J., Schwandner, F. M., Sun, Y., O'Dell, C. W., Frankenberg, C., Taylor, T., Fisher, B., Osterman, G. B., Wunch, D., Hakkarainen, J., Tamminen, J., and Weir, B.: The Orbiting Carbon Observatory-2 early science investigations of regional carbon dioxide fluxes, Science (80-.)., 358, https://doi.org/10.1126/science.aam5745, 2017.

Feely, R. A., Wanninkhof, R., Takahashi, T., & Tans, P. (1999). Influence of El Niño on the equatorial Pacific contribution to atmospheric CO2 accumulation. Nature 1999 398:6728, 398(6728), 597–601. https://doi.org/10.1038/19273

Feldman, A. F., Zhang, Z., Yoshida, Y., Chatterjee, A., and Poulter, B.: Using Orbiting Carbon Observatory-2 (OCO-2) column CO2 retrievals to rapidly detect and estimate biospheric surface carbon flux anomalies, Atmos. Chem. Phys., 23, 1545–1563, https://doi.org/10.5194/acp-23-1545-2023, 2023.

Friedlingstein, P., Jones, M. W., O'Sullivan, M., Andrew, R. M., Bakker, D. C. E., Hauck, J., Le Quéré, C., Peters, G. P., Peters, W., Pongratz, J., Sitch, S., Canadell, J. G., Ciais, P., Jackson, R. B., Alin, S. R., Anthoni, P., Bates, N. R., Becker, M., Bellouin, N., Bopp, L., Chau, T. T. T., Chevallier, F., Chini, L. P., Cronin, M., Currie, K. I., Decharme, B., Djeutchouang, L. M., Dou, X., Evans, W., Feely, R. A., Feng, L., Gasser, T., Gilfillan, D., Gkritzalis, T., Grassi, G., Gregor, L., Gruber, N., Gürses, Ö., Harris, I., Houghton, R. A., Hurtt, G. C., Iida, Y., Ilyina, T., Luijkx, I. T., Jain, A., Jones, S. D., Kato, E., Kennedy, D., Klein Goldewijk, K., Knauer, J., Korsbakken, J. I., Körtzinger, A., Landschützer, P., Lauvset, S. K., Lefèvre, N., Lienert, S., Liu, J., Marland, G., McGuire, P. C., Melton, J. R., Munro, D. R., Nabel, J. E. M. S., Nakaoka, S.-I., Niwa, Y., Ono, T., Pierrot, D., Poulter, B., Rehder, G., Resplandy, L., Robertson, E., Rödenbeck, C., Rosan, T. M., Schwinger, J., Schwingshackl, C., Séférian, R., Sutton, A. J., Sweeney, C., Tanhua, T., Tans, P. P., Tian, H., Tilbrook, B., Tubiello, F., van der Werf, G. R., Vuichard, N., Wada, C., Wanninkhof, R., Watson, A. J., Willis, D., Wiltshire, A. J., Yuan, W., Yue, C., Yue, X., Zaehle, S., and Zeng, J.: Global Carbon Budget 2021, Earth Syst. Sci. Data, 14, 1917–2005, https://doi.org/10.5194/essd-14-1917-2022, 2022a.

Friedlingstein, P., O'Sullivan, M., Jones, M. W., Andrew, R. M., Gregor, L., Hauck, J., Le Quéré, C., Luijkx, I. T., Olsen, A., Peters, G. P., Peters, W., Pongratz, J., Schwingshackl, C., Sitch, S., Canadell, J. G., Ciais, P., Jackson, R. B., Alin, S. R., Alkama, R., Arneth, A., Arora, V. K., Bates, N. R., Becker, M., Bellouin, N., Bittig, H. C., Bopp, L., Chevallier, F., Chini, L. P., Cronin, M., Evans, W., Falk, S., Feely, R. A., Gasser, T., Gehlen, M., Gkritzalis, T., Gloege, L., Grassi, G., Gruber, N., Gürses, Ö., Harris, I., Hefner, M., Houghton, R. A., Hurtt, G. C., Iida, Y., Ilyina, T., Jain, A. K., Jersild, A., Kadono, K., Kato, E., Kennedy, D., Klein Goldewijk, K., Knauer, J., Korsbakken, J. I., Landschützer, P., Lefèvre, N., Lindsay, K., Liu, J., Liu, Z., Marland, G., Mayot, N., McGrath, M. J., Metzl, N., Monacci, N. M., Munro, D. R., Nakaoka, S.-I., Niwa, Y., O'Brien, K., Ono, T., Palmer, P. I., Pan, N., Pierrot, D., Pocock, K., Poulter, B., Resplandy, L., Robertson, E., Rödenbeck, C., Rodriguez, C., Rosan, T. M., Schwinger, J., Séférian, R., Shutler, J. D., Skjelvan, I., Steinhoff, T., Sun, Q., Sutton, A. J., Sweeney, C., Takao, S., Tanhua, T., Tans, P. P., Tian, X., Tian, H., Tilbrook, B., Tsujino, H., Tubiello, F., van der Werf, G. R., Walker, A. P., Wanninkhof, R., Whitehead, C., Willstrand Wranne, A., Wright, R., Yuan, W., Yue, C., Yue, X., Zaehle, S., Zeng, J., and Zheng, B.: Global Carbon Budget 2022, Earth Syst. Sci. Data, 14, 4811–4900, https://doi.org/10.5194/essd-14-4811-2022, 2022b.

Hall, B. D., Crotwell, A. M., Kitzis, D. R., Mefford, T., Miller, B. R., Schibig, M. F., and Tans, P. P.: Revision of the World Meteorological Organization Global Atmosphere Watch (WMO/GAW) CO2 calibration scale, Atmos. Meas. Tech., 14, 3015–3032, https://doi.org/10.5194/amt-14-3015-2021, 2021.

Houweling, S., Badawy, B., Baker, D. F., Basu, S., Belikov, D., Bergamaschi, P., Bousquet, P., Broquet, G., Butler, T., Canadell, J. G., Chen, J., Chevallier, F., Ciais, P., Collatz, G. J., Denning, S., Engelen, R., Enting, I. G., Fischer, M. L., Fraser, A., Gerbig, C., Gloor, M., Jacobson, A. R., Jones, D. B. A., Heimann, M., Khalil, A., Kaminski, T., Kasibhatla, P. S., Krakauer, N. Y., Krol, M., Maki, T., Maksyutov, S., Manning, A., Meesters, A., Miller, J. B., Palmer, P. I., Patra, P., Peters, W., Peylin, P., Poussi, Z., Prather, M. J., Randerson, J. T., Röckmann, T., Rödenbeck, C., Sarmiento, J. L., Schimel, D. S., Scholze, M., Schuh, A., Suntharalingam, P., Takahashi, T., Turnbull, J., Yurganov, L., and Vermeulen, A.: Iconic CO2 Time Series at Risk, Science (80-.)., 337, 1038–1040, https://doi.org/10.1126/science.337.6098.1038-b, 2012.

Karion, A., Sweeney, C., Tans, P., and Newberger, T., (2010) AirCore: An Innovative Atmospheric Sampling System, Journal of Atmospheric and Oceanic Technology, Nov. 2010, doi: 10.1175/2010JTECHA1448.1.

Keeling, C.D.: The Concentration and Isotopic Abundances of Carbon Dioxide in the Atmosphere. Tellus, 12: 200-203. https://doi.org/10.1111/j.2153-3490.1960.tb01300.x, 1960

Kiel, M., O'Dell, C. W., Fisher, B., Eldering, A., Nassar, R., MacDonald, C. G., and Wennberg, P. O.: How bias correction goes wrong: measurement of XCO2 affected by erroneous sur- face pressure estimates, Atmos. Meas. Tech., 12, 2241–2259, https://doi.org/10.5194/amt-12-2241-2019, 2019.

Knorr, W.: Is the airborne fraction of anthropogenic CO2 emissions increasing?, Geophys. Res. Lett., 36, 1–5, https://doi.org/10.1029/2009GL040613, 2009.

Lan, X., Tans, P. and K.W. Thoning: Trends in globally-averaged CO2 determined from NOAA Global Monitoring Laboratory measurements. Version 2023-11 https://doi.org/10.15138/9N0H-ZH07 last access: 15 November 2023.

Laughner, J. L., Roche, S., Kiel, M., Toon, G. C., Wunch, D., Baier, B. C., Biraud, S., Chen, H., Kivi, R., Laemmel, T., McK- ain, K., Quéhé, P.-Y., Rousogenous, C., Stephens, B. B., Walker, K., and Wennberg, P. O.: A new algorithm to generate a pri- ori trace gas profiles for the GGG2020 retrieval algorithm, At- mos. Meas. Tech., 16, 1121–1146, https://doi.org/10.5194/amt- 16-1121-2023, 2023a.

Laughner, J. L., Toon, G. C., Mendonca, J., Petri, C., Roche, S., Wunch, D., Blavier, J.-F., Griffith, D. W. T., Heikkinen, P., Keeling, R. F., Kiel, M., Kivi, R., Roehl, C. M., Stephens, B. B., Baier, B. C., Chen, H., Choi, Y., Deutscher, N. M., DiGangi, J. P., Gross, J., Herkommer, B., Jeseck, P., Laemmel, T., Lan, X., McGee, E., McKain, K., Miller, J., Morino, I., Notholt, J., Ohyama, H., Pollard, D. F., Rettinger, M., Riris, H., Rousogenous, C., Sha, M. K., Shiomi, K., Strong, K.,

Sussmann, R., Té, Y., Velazco, V. A., Wofsy, S. C., Zhou, M., and Wennberg, P. O.: The Total Carbon Column Observing Network's GGG2020 Data Version, Earth Syst. Sci. Data Discuss. [preprint], https://doi.org/10.5194/essd-2023-331, in review, 2023b.

Laughner, J. L., Neu, J. L., Schimel, D., Wennberg, P. O., Barsanti, K., Bowman, K. W., Chatterjee, A., Croes, B. E., Fitzmaurice, H. L., Henze, D. K., Kim, J., Kort, E. A., Liu, Z., Miyazaki, K., Turner, A. J., Anenberg, S., Avise, J., Cao, H., Crisp, D., De Gouw, J., Eldering, A., Fyfe, J. C., Goldberg, D. L., Gurney, K. R., Hasheminassab, S., Hopkins, F., Ivey, C. E., Jones, D. B. A., Liu, J., Lovenduski, N. S., Martin, R. V., McKinley, G. A., Ott, L., Poulter, B., Ru, M., Sander, S. P., Swart, N., Yung, Y. L., and Zeng, Z. C.: Societal shifts due to COVID-19 reveal large-scale complexities and feedbacks between atmospheric chemistry and climate change, Proc. Natl. Acad. Sci. U. S. A., 118, e2109481118, https://doi.org/10.1073/PNAS.2109481118/SUPPL_FILE/PNAS.2109481118.SD02.XLSX, 2021.

Lorente, A., Borsdorff, T., Butz, A., Hasekamp, O., aan de Brugh, J., Schneider, A., Wu, L., Hase, F., Kivi, R., Wunch, D., Pollard, D. F., Shiomi, K., Deutscher, N. M., Velazco, V. A., Roehl, C. M., Wennberg, P. O., Warneke, T., and Landgraf, J.: Methane retrieved from TROPOMI: improvement of the data product and validation of the first 2 years of measurements, Atmos. Meas. Tech., 14, 665–684, https://doi.org/10.5194/amt-14-665-2021, 2021.

Liu, J., Bowman, K. W., Schimel, D., Parazoo, N. C., Jiang, Z., Lee, M., Anthony Bloom, A., Wunch, D., Frankenberg, C., Sun, Y., O'Dell, C. W., Gurney, K. R., Menemenlis, D., Gierach, M., Crisp, D., and Eldering, A.: Contrasting carbon cycle responses of the tropical continents to the 2015–2016 El Niño, Science (80-.)., 362, https://doi.org/10.1126/science.aat1211, 2018.

Masarie, K. A. and Tans, P. P.: Extension and integration of atmospheric carbon dioxide data into a globally consistent measurement record, J. Geophys. Res., 100, 11593, https://doi.org/10.1029/95jd00859, 1995.

NOAA NOAA/GML calculation of global means available at: https://gml.noaa.gov/ccgg/about/global_means.html last access: 14 September 2023.

OCO Science Team, Gunson, M., and Eldering, A.: OCO-2 Level 2 bias-corrected XCO2 and other select fields from the full- physics retrieval aggregated as daily files, Retrospective processing V10r, Goddard Earth Sciences Data and Information Services Center (GES DISC), Greenbelt, MD, USA [data set], https://doi.org/10.5067/E4E140XDMPO2, 2020.

Oda, T., Maksyutov, S., and Andres, R. J.: The Open-source Data Inventory for Anthropogenic CO2, version 2016 (ODIAC2016): a global monthly fossil fuel CO2 gridded emissions data product for tracer transport simulations and surface flux inversions, Earth Syst. Sci. Data, 10, 87–107, https://doi.org/10.5194/essd-10-87-2018, 2018.

O'Dell, C. W., Eldering, A., Wennberg, P. O., Crisp, D., Gunson, M. R., Fisher, B., Frankenberg, C., Kiel, M., Lindqvist, H., Mandrake, L., Merrelli, A., Natraj, V., Nelson, R. R., Osterman, G. B., Payne, V. H., Taylor, T. E., Wunch, D., Drouin, B. J., Oyafuso, F., Chang, A., McDuffie, J., Smyth, M., Baker, D. F., Basu, S., Chevallier, F., Crowell, S. M. R., Feng, L., Palmer, P. I., Dubey, M., García, O. E., Griffith, D. W. T., Hase, F., Iraci, L. T., Kivi, R., Morino, I., Notholt, J., Ohyama, H., Petri, C., Roehl, C. M., Sha, M. K., Strong, K., Sussmann, R., Te, Y., Uchino, O., and Velazco, V. A.: Improved retrievals of carbon dioxide from Orbiting Carbon Observatory-2 with the version 8 ACOS algorithm, Atmos. Meas. Tech., 11, 6539–6576, https://doi.org/10.5194/amt-11-6539-2018, 2018.

O'Dell, C. W., Eldering, A., Wennberg, P. O., Crisp, D., Gunson, M. R., Fisher, B., Frankenberg, C., Kiel, M., Lindqvist, H., Man- drake, L., Merrelli, A., Natraj, V., Nelson, R. R., Osterman, G. B., Payne, V. H., Taylor, T. E., Wunch, D., Drouin, B. J., Oyafuso, F., Chang, A., McDuffie, J., Smyth, M., Baker, D. F., Basu, S., Chevallier, F., Crowell, S. M. R., Feng, L., Palmer, P. I., Dubey, M., García, O. E., Griffith, D. W. T., Hase, F., Iraci, L. T., Kivi, R., Morino, I., Notholt, J., Ohyama, H., Petri, C., Roehl, C. M., Sha, M. K., Strong, K., Sussmann, R., Te, Y., Uchino, O., and Ve- lazco, V. A.: Improved retrievals of carbon dioxide from Orbiting Carbon Observatory-2 with the version 8 ACOS algorithm, At- mos. Meas. Tech., 11, 6539–6576, https://doi.org/10.5194/amt- 11-6539-2018, 2018.

Pandey, S., Houweling, S., Krol, M., Aben, I., and Röckmann, T.: On the use of satellite-derived CH4: CO2 columns in a joint inversion of CH4 and CO2 fluxes, Atmos. Chem. Phys., 15, 8615–8629, https://doi.org/10.5194/acp-15-8615-2015, 2015.

Pandey, S., Houweling, S., Krol, M., and Aben, I.: Influence of Atmospheric Transport on Estimates of Variability in the Global Methane Burden Geophysical Research Letters, Geophys. Res. Lett., 46, 2302–2311, https://doi.org/10.1029/2018GL081092, 2019.

Peiro, H., Crowell, S., Schuh, A., Baker, D. F., O'Dell, C., Jacobson, A. R., Chevallier, F., Liu, J., Eldering, A., Crisp, D., Deng, F., Weir, B., Basu, S., Johnson, M. S., Philip, S., and Baker, I.: Four years of global carbon cycle observed from the Orbiting Carbon Observatory 2 (OCO-2) version 9 and in situ data and comparison to OCO-2 version 7, Atmos. Chem. Phys., 22, 1097–1130, https://doi.org/10.5194/acp-22-1097-2022, 2022.

Schneising, O., Buchwitz, M., Reuter, M., Bovensmann, H., Burrows, J. P., Borsdorff, T., Deutscher, N. M., Feist, D. G., Griffith, D. W. T., Hase, F., Hermans, C., Iraci, L. T., Kivi, R., Landgraf, J., Morino, I., Notholt, J., Petri, C., Pollard, D. F., Roche, S., Shiomi, K., Strong, K., Sussmann, R., Velazco, V. A., Warneke, T., and Wunch, D.: A scientific algorithm to simultaneously retrieve carbon monoxide and methane from TROPOMI onboard Sentinel-5 Precursor, Atmos. Meas. Tech., 12, 6771–6802, https://doi.org/10.5194/amt-12-6771-2019, 2019.

Schuldt, K. N., Mund, M., Luijkx, I. T., et al.: Multi-laboratory compilation of atmospheric carbon dioxide data for the period 1957–2019, obspack_co2_1_GLOBALVIEWplus_v6.1_2021-03-01, NOAA Earth System Research Laboratory, Global Monitoring Laboratory [data set], https://doi.org/10.25925/20210801, 2021.

Taylor, T. E., O'Dell, C. W., Baker, D., Bruegge, C., Chang, A., Chapsky, L., Chatterjee, A., Cheng, C., Chevallier, F., Crisp, D., Dang, L., Drouin, B., Eldering, A., Feng, L., Fisher, B., Fu, D., Gunson, M., Haemmerle, V., Keller, G. R., Kiel, M., Kuai, L., Kurosu, T., Lambert, A., Laughner, J., Lee, R., Liu, J., Mandrake, L., Marchetti, Y., McGarragh, G., Merrelli, A., Nelson, R. R., Osterman, G., Oyafuso, F., Palmer, P. I., Payne, V. H., Rosenberg, R., Somkuti, P., Spiers, G., To, C., Weir, B., Wennberg, P. O., Yu, S., and Zong, J.: Evaluating the consistency between OCO-2 and OCO-3 XCO 2 estimates derived from the NASA ACOS version 10 retrieval algorithm , Atmos. Meas. Tech., 16, 3173–3209, https://doi.org/10.5194/amt-16-3173-2023, 2023.

Tans, P. P., T. J. Conway and T. Nakazawa; Latitudinal distribution of the sources and sinks of atmospheric carbon dioxide derived from surface observations and atmospheric transport model, J. of Geophys. Res., 94., 5151-5172. 1989.

Thoning, K.W., P.P. Tans, and W.D. Komhyr,: Atmospheric carbon dioxide at Mauna Loa Observatory, 2. Analysis of the NOAA/GMCC data, 1974 1985., J. Geophys. Res. ,94, 8549 8565., 1989.

Tsutsumi, Y.; Mori, K.; Hirahara, T. et al. Technical Report of Global Analysis Method for Major Greenhouse Gases by the World Data Center for Greenhouse Gases (WMO/TD-No. 1473). GAW Report No. 184. World Meteorological Organization (WMO): Geneva, 2009. Available at https://library.wmo.int/idurl/4/47548 last access: 14 September 2023

NIES GOSAT Project: Recent global CO2, available at https://www.gosat.nies.go.jp/en/recent-global-co2.html last access: 14 September 2023

Weir, B., Crisp, D., Dell, C. W. O., Basu, S., Chatterjee, A., Kolassa, J., Oda, T., Pawson, S., Poulter, B., Zhang, Z., Ciais, P., Davis, S. J., Liu, Z., and Ott, L. E.: Regional impacts of COVID-19 on carbon dioxide detected worldwide from space, Science Advances, 7, eabf9415, 2021.

Weir, B., Ott, L., and OCO-2 Science Team (2022), OCO-2 GEOS Level 3 daily, 0.5x0.625 assimilated CO2 V10r, Greenbelt, MD, USA, Goddard Earth Sciences Data and Information Services Center (GES DISC), https://doi.org/10.5067/Y9M4NM9MPCGH Accessed: (14 September 2023)

Williams, A. P., Cook, B. I., and Smerdon, J. E.: Rapid intensification of the emerging southwestern North American megadrought in 2021, Nat. Clim. Change, 12, 232–234, https://doi.org/10.1038/s41558-022-01290-z, 2022.

Wolter, Klaus, and Michael S. Timlin. "El NiñO/Southern Oscillation Behaviour since 1871 As Diagnosed in an Extended Multivariate ENSO Index (MEI.Ext)." International Journal of Climatology, vol. 31, no. 7, 2011, pp. 1074-1087, https://doi.org/10.1002/joc.2336. (Accessed 14 September 2023)

WMO GREENHOUSE GAS BULLETIN No. 18 The State of Greenhouse Gases in the Atmosphere Based on Global Observations through 2021, Sulphur, 5–8, 2022. Available at: https://library.wmo.int/records/item/58743-no-18-26-october-2022 (last access 14 September 2023)

Wu, Z., Vermeulen, A., Sawa, Y., Karstens, U., Peters, W., de Kok, R., Lan, X., Nagai, Y., Ogi, A., and Tarasova, O.: Investigating the differences in calculating global mean surface CO2 abundance: the impact of analysis methodologies and site selection, Atmos. Chem. Phys., 24, 1249–1264, https://doi.org/10.5194/acp-24-1249-2024, 2024.

Wunch, D., Wennberg, P. O., Osterman, G., Fisher, B., Naylor, B., Roehl, C. M., O'Dell, C., Mandrake, L., Viatte, C., Kiel, M., Griffith, D. W. T., Deutscher, N. M., Velazco, V. A., Notholt, J., Warneke, T., Petri, C., De Maziere, M., Sha, M. K., Sussmann, R., Rettinger, M., Pollard, D., Robinson, J., Morino, I., Uchino, O., Hase, F., Blumenstock, T., Feist, D. G., Arnold, S. G., Strong, K., Mendonca, J., Kivi, R., Heikkinen, P., Iraci, L., Podolske, J., Hillyard, P. W., Kawakami, S., Dubey, M. K., Parker, H. A., Sepulveda, E., García, O. E., Te, Y., Jeseck, P., Gunson, M. R., Crisp, D., and Eldering, A.: Comparisons of the Orbiting Carbon Observatory-2 (OCO-2) measurements with TCCON, Atmos. Meas. Tech., 10, 2209–2238, https://doi.org/10.5194/amt-10-2209-2017, 2017.

Van Marle, M. J. E., van Wees, D., Houghton, R. A., Field, R. D., Verbesselt, J., and van der Werf, Guido. R.: New land-use-change emissions indicate a declining CO2 airborne fraction, Nature, 603, 450–454, https://doi.org/10.1038/s41586-021-04376-4, 2022.